ANTIPSYCHOTIC DRUGS SELECTIVELY DECORRELATE LONG-RANGE INTERACTIONS IN DEEP CORTICAL LAYERS

Matthias Heindorf[1] & Georg B. Keller[1,2,3]

[1]Friedrich Miescher Institute for Biomedical Research, Basel, Switzerland
[2]Faculty of Science, University of Basel, Basel, Switzerland
[3]Lead contact, correspondence to: georg.keller@fmi.ch

Psychosis is characterized by a diminished ability of the brain to distinguish externally driven activity patterns from self-generated activity patterns. Antipsychotic drugs are a class of small molecules with relatively broad binding affinity for a variety of neuromodulator receptors that, in humans, can prevent or ameliorate psychosis. How these drugs influence the function of cortical circuits, and in particular their ability to identify self-generated activity patterns, is still largely unclear. Here we used widefield calcium imaging to determine the cell type specific functional effects of antipsychotic drugs in mouse dorsal cortex during visuomotor integration. By comparing cell type specific activation patterns between locomotion onsets that were experimentally coupled to self-generated visual feedback and locomotion onsets that were not coupled, we show that deep cortical layers were differentially activated in these two conditions. We then show that the antipsychotic drug clozapine disrupted visuomotor integration at locomotion onsets also primarily in deep cortical layers. Given that one of the key components of visuomotor integration in cortex is long-range cortico-cortical connections, we tested whether the effect of clozapine was detectable in the correlation structure of activity patterns across dorsal cortex. We found that clozapine as well as two other antipsychotic drugs, aripiprazole and haloperidol, resulted in a strong reduction in correlations of layer 5 activity between cortical areas and impaired the spread of visuomotor prediction errors generated in visual cortex. Our results are consistent with the interpretation that a major functional effect of antipsychotic drugs is an alteration of the activation of internal representations as a consequence of reduced long-range layer 5 mediated communication.

**** Dear reader, please note this manuscript is formatted in a standard submission format, and all statistical information is provided in Table S1. ****

INTRODUCTION

Under normal conditions, self-generated movements are coupled to sensory feedback in different modalities. Locomotion, for example, is coupled to proprioceptive feedback from muscle

movements, somatosensory and auditory feedback from touching the ground, vestibular feedback from translational acceleration, and visual feedback in the form of expanding visual flow. This coupling is key to our brain's ability to learn internal models of the world (Jordan and Rumelhart, 1992). Internal models are the transformations between cortical areas and can be used to predict the sensory consequences of movement. Hallucinations and delusions can be explained as a misconfiguration of these internal models: inaccurate predictions of the sensory consequences of movements can result in self-generated activity that is not correctly distinguished from externally driven activity (Fletcher and Frith, 2009; Frith, 2005).

Self-generated movements result in broad activation of most regions of the brain (Musall et al., 2019; Stringer et al., 2019), including some primary sensory areas like visual cortex (Keller et al., 2012; Saleem et al., 2013) where they have been shown to depend on visual context (Pakan et al., 2016). The framework of predictive processing postulates that in cortex, these movement related signals are internal model based predictions of the sensory consequences of movement that are compared to externally generated bottom-up input to compute prediction errors (Jiang and Rao, 2021; Keller and Mrsic-Flogel, 2018). Evidence for this interpretation has mainly come from the discovery of movement related prediction error responses in a variety of different cortical regions and species (Attinger et al., 2017; Audette et al., 2021; Ayaz et al., 2019; Eliades and Wang, 2008; Heindorf et al., 2018; Keller et al., 2012; Keller and Hahnloser, 2009; Stanley and Miall, 2007; Zmarz and Keller, 2016), and the observation that top-down inputs from motor areas of cortex appear to convey movement related predictions of sensory input to sensory areas of cortex (Leinweber et al., 2017; Schneider et al., 2018). The neurons on which the opposing bottom-up input and top-down prediction converge are referred to as prediction error neurons and are thought to reside primarily in layer 2/3 (L2/3) of cortex (Jordan and Keller, 2020). To complete the circuit, there also needs to be a population of neurons that integrate over prediction error responses. These are referred to as internal representation neurons. It is still unclear which cortical neuron type functions as internal representation neurons, but based on anatomical arguments it has been speculated that they can be found in deep cortical layers (Bastos et al., 2012).

In humans, externally driven and self-generated activity patterns can be experimentally separated at least partially, for example, by showing subjects a visual stimulus and later asking them to visualize the same stimulus (Le Bihan et al., 1993). This type of experiment is considerably more difficult to perform in animals. Using movement as a proxy for self-generated activity patterns, however, using a virtual environment, we can compare a condition in which self-generated and externally generated activity patterns are correlated to a condition in which they are not. In the visual system, we can use

66 a virtual reality environment to experimentally couple or decouple locomotion from visual flow
67 feedback. We will refer to the former as a closed loop condition and to the latter as an open loop
68 condition. Assuming the predictive processing model is correct, we should find differences in the
69 activation patterns in dorsal cortex in response to locomotion onsets as a function of whether they
70 occurred with or without coupled visual flow feedback. Both prediction error neurons as well as
71 internal representation neurons should respond differentially. Thus, we set out to investigate
72 whether there are differences between closed and open loop activation patterns of mouse dorsal
73 cortex, and whether these differences are neuron type specific. If hallucinations are indeed the
74 result of aberrant activation of internal representations, possibly as a result of misconfigured
75 internal models, antipsychotic drugs should alter the differential activation patterns in these
76 neurons.

77 **RESULTS**

78 **Tlx3 positive layer 5 (L5) intratelencephalic (IT) neurons distinguished closed and open loop**
79 **visuomotor coupling**

80 To investigate neuron type specific differences in activity patterns at locomotion onsets with and
81 without self-generated visual feedback in mouse dorsal cortex, we quantified locomotion onset
82 activity using widefield calcium imaging (Wekselblatt et al., 2016). A GCaMP variant was expressed
83 using either a retro-orbital injection of an AAV-PHP.eB vector (Chan et al., 2017), or a cross between
84 a Cre line and the Ai148 GCaMP6 reporter line (Daigle et al., 2018) (see Methods; **Figure 1A**, **Table**
85 **S2**). Mice expressed a GCaMP variant either brain wide (C57BL/6), or in genetically identified subsets
86 of excitatory or inhibitory neurons using Cre driver lines. Please note, we use the term 'brain wide'
87 here to describe an expression pattern that was determined by the intersection of the AAV-PHP.eB
88 tropism and the expression pattern of EF1α or hSyn1 promoters but that was otherwise brain wide
89 (see Discussion). We used Emx1-Cre mice to target expression to cortical excitatory neurons (Gorski
90 et al., 2002), Cux2-CreERT2 mice to target expression to L2/3 and L4 layer excitatory neurons (Franco
91 et al., 2012), Scnn1a-Cre mice to target expression to a subset of L4 excitatory neurons (Madisen et
92 al., 2010), Tlx3-Cre mice to target expression to a subset of L5 IT neurons (Gerfen et al., 2013), and
93 Ntsr1-Cre mice to target expression to a subset of L6 excitatory neurons (Gong et al., 2007). To
94 target subpopulations of inhibitory neurons, we used PV-Cre (Hippenmeyer et al., 2005), VIP-Cre
95 (Taniguchi et al., 2011), and SST-Cre mice (Taniguchi et al., 2011) (see Methods). Prior to the start of
96 the imaging experiments, mice were implanted with a crystal skull cranial window (Kim et al., 2016).
97 We used crystal skull preparations as we found that hemodynamic artifacts were smaller in this
98 preparation compared to those observed in clear skull preparations (**Figures S1A and S1B**). For all

experiments, mice were head fixed and free to locomote on a spherical treadmill (**Figure 1B**). Activity from dorsal cortex was imaged while mice were in a closed loop visuomotor condition, in which locomotion on the spherical treadmill controlled forward movement in a virtual corridor. Following this, mice were exposed to an open loop condition during which mice were presented with a replay of the visual flow they had self-generated in the preceding closed loop condition.

We first compared locomotion onset responses in the closed loop condition to those in the open loop condition in mice that expressed GCaMP brain wide (C57BL/6). Consistent with previous findings (Musall et al., 2019; Stringer et al., 2019), we found that locomotion onset resulted in broad activation across most of dorsal cortex in both conditions (**Figure 1C**). However, comparing locomotion onsets in mice that expressed GCaMP6 only in Tlx3 positive L5 IT neurons, we found that the activation pattern was strikingly different between closed and open loop conditions (**Figure 1D**). While locomotion onset in the open loop condition resulted in an increase in activity across dorsal cortex similar to that observed in C57BL/6 mice with brain wide GCaMP expression, locomotion onset in the closed loop condition resulted in a very different activation pattern: In posterior parts of dorsal cortex, the activity decreased, while in anterior parts of the dorsal cortex, the activity increased. To quantify these activation patterns across mice, we selected six regions of interest: primary visual cortex (V1), antero-medial secondary visual cortex (V2am), retrosplenial cortex (RSC), primary motor cortex (M1), anterior cingulate cortex at the level of bregma (A24b), and secondary motor cortex (M2) (**Figure 1E**). In C57BL/6 mice that expressed GCaMP brain wide, closed loop locomotion onset resulted in similar activity patterns across these six regions (**Figure 1F**). This activity pattern was not markedly different from that observed during locomotion onsets in an open loop condition (**Figure 1G**). To quantify the contribution of visual flow onset to the closed loop locomotion onset activity, we measured responses to visual flow onsets that occurred in the absence of locomotion in the open loop condition (**Figure 1H**). In C57BL/6 mice with brain wide GCaMP expression, visual flow onsets resulted in responses that were small compared to those observed during locomotion onset, even in V1. Note that a visual flow onset is a relatively weak visual stimulus compared to a drifting grating stimulus. A grating stimulus is typically composed of a gray screen or a standing grating stimulus that suddenly transitions to a drifting grating, and thus the visual flow undergoes a very high acceleration. A visual flow onset in an open loop condition is the replay of previously self-generated visual flow and thus exhibits much lower visual flow acceleration. The absence of a strong visual flow onset response in C57BL/6 mice that expressed GCaMP brain wide is consistent with a high similarity of closed and open loop locomotion onset responses.

131 In mice that expressed GCaMP6 in Tlx3 positive L5 IT neurons, the closed loop locomotion onset
132 patterns differed markedly when compared across the six regions of interest (**Figure 1I**). Moreover,
133 these activation patterns were different from those observed during open loop locomotion onsets
134 (**Figure 1J**). While these responses could partially be explained by hemodynamic occlusion, the time
135 course of hemodynamic occlusion in Tlx3-Cre mice that expressed eGFP in L5 IT neurons was similar
136 to that observed in C57BL/6 mice that expressed eGFP brain wide and mainly resulted in a decrease
137 of fluorescence (**Figures S1C and S1D**). In Tlx3 positive L5 IT neurons, open loop visual flow onsets
138 that occurred in the absence of locomotion resulted in quantifiable responses in V1 and V2am
139 (**Figure 1K**), but the closed loop locomotion onset responses in V1 could not be explained by the sum
140 of locomotion and visual flow onset responses (**Figure S2**). Most of the widefield signals we record
141 here likely originate in compartments in superficial layers which are composed of axons and
142 dendrites of local neurons, and long-range inputs (Allen et al., 2017) (see Discussion). To test how
143 well the widefield signals recorded in V1 reflected local somatic activity in V1, we repeated the
144 experiments using two-photon calcium imaging of somatic activity in Tlx3 positive L5 IT neurons. We
145 found that while there were differences between the responses measured with widefield imaging
146 and those measured at the soma, both for locomotion onset responses and visual responses, these
147 differences did not change our conclusions (**Figure S3**).

148 We then repeated these experiments and analyses for the other excitatory and inhibitory cortical
149 neuron types (**Figure S4**). For each neuron type, we quantified the similarity of the activity patterns
150 associated with closed and open loop locomotion onsets by calculating the correlation coefficient
151 between the activity traces in a window around locomotion onset (-5 s to +3 s) and averaging across
152 regions of interest (see Methods). We found the highest similarity between closed and open loop
153 locomotion onsets in C57BL/6 mice that expressed GCaMP brain wide and in mice that expressed
154 GCaMP6 in PV positive interneurons, and the similarity was lowest in mice that expressed GCaMP6
155 in Tlx3 positive L5 IT and Ntsr1 positive L6 excitatory neurons (**Figure 1L**). Thus, excitatory neurons of
156 deep cortical layers exhibited the strongest differences between closed and open loop locomotion
157 related activation. The remarkable aspect of these findings is not that there are differences between
158 closed and open loop locomotion onsets, particularly in visual regions of cortex one would perhaps
159 expect to find differences, but that these differences are larger specifically in the deep cortical
160 layers.

161 To quantify how the interaction between locomotion and visual flow feedback changes across dorsal
162 cortex, we computed correlations between calcium activity and locomotion speed for each region of
163 interest, for closed and open loop conditions separately. In C57BL/6 mice that expressed GCaMP

164 brain wide, this correlation was comparable between closed and open loop conditions, was highest
165 in posterior regions of dorsal cortex, and lower in more anterior regions (**Figures 2A and 2B**). In mice
166 that expressed GCaMP6 in Tlx3 positive L5 IT neurons, the correlation between locomotion speed
167 and calcium activity in the closed loop condition was negative in posterior regions of dorsal cortex
168 and positive in anterior regions. Conversely, in open loop conditions, the correlation was positive
169 throughout dorsal cortex (**Figures 2C and 2D**). To test whether it was the coupling of visual flow that
170 resulted in a reduction of the correlation in the closed loop condition or whether the presence of an
171 uncoupled visual stimulus resulted in an increase of correlation in the open loop condition, we also
172 compared these correlations to those observed when mice were locomoting in relative darkness
173 (see Methods). In C57BL/6 mice that expressed GCaMP brain wide, the correlation of calcium activity
174 with locomotion in darkness was indistinguishable from that in closed or open loop (**Figure 2B**). In
175 mice that expressed GCaMP6 in Tlx3 positive L5 IT neurons, an interesting pattern emerged. In visual
176 regions of dorsal cortex, the correlation between locomotion speed and calcium activity in relative
177 darkness resembled that observed in open loop conditions, while in frontal regions, it resembled
178 that observed in closed loop conditions. In visual regions, the coupling of visual flow resulted in a
179 reduction of correlation, while in frontal regions the presence of an uncoupled visual stimulus
180 resulted in an increase of correlations. Thus, the difference between closed and open loop
181 conditions likely had different origins in visual and frontal regions of dorsal cortex. Overall, we
182 concluded that the coupling of locomotion and resulting visual flow feedback not only activated Tlx3
183 positive L5 IT neurons differentially but did so throughout dorsal cortex, well beyond visual regions.

184 **Visuomotor prediction errors originated in visual cortical regions and had opposing effects on Tlx3**
185 **positive L5 IT activity**

186 A consequence of the natural coupling of locomotion and visual flow feedback is that movements
187 are a good predictor of self-generated sensory feedback. In our closed loop experiments, forward
188 locomotion was a strong predictor of backward visual flow. It has been speculated that such
189 predictions are used to compute prediction errors in L2/3 of cortex (Jordan and Keller, 2020).
190 Prediction errors come in two variants: Positive prediction errors that signal more visual flow than
191 predicted and negative prediction errors that signal less visual flow than predicted (Keller and Mrsic-
192 Flogel, 2018; Rao and Ballard, 1999). To probe for negative and positive prediction error signals, we
193 quantified the responses to visuomotor mismatch events and to unexpected visual stimuli
194 (representing less and more visual flow input than expected, respectively). Visuomotor mismatch
195 was introduced by briefly (1 s) halting visual flow during self-generated feedback in the closed loop
196 condition. Visual responses were elicited by presenting drifting grating stimuli to a passively

observing mouse (see Methods). Please note, both types of prediction errors can be probed using a variety of stimuli, but the two we are using here, in our experience, are the most robust at eliciting strong responses in V1. In C57BL/6 mice that expressed GCaMP brain wide, both visuomotor mismatch and grating stimuli resulted in increases of activity that were strongest and appeared first in visual regions of dorsal cortex (**Figures 3A-3C**). In mice that expressed GCaMP6 in Tlx3 positive L5 IT neurons, visuomotor mismatch resulted in an increase of activity in V1, while grating onsets resulted in a decrease of activity in V1 (**Figures 3D-3F**). Thus, in dorsal cortex, both mismatch and drifting grating stimuli primarily activated visual cortex but resulted in opposing activation patterns in Tlx3 positive L5 IT neurons. An increase in activity to negative prediction errors and a decrease to positive prediction errors would be consistent with either a population of negative prediction error neurons or a type of internal representation neuron (Rao and Ballard, 1999). Given that L5 neurons in V1 do not exhibit the opposing influence of top-down and bottom-up inputs necessary to compute prediction errors (Jordan and Keller, 2020), we speculated that Tlx3 positive L5 IT neurons might function as a type of internal representation neuron.

The antipsychotic drug clozapine alters visuomotor integration in L5

The activation of an internal representation is the brain's best guess at what the stimuli in the environment are. We speculated that the activation of such an internal representation would be particularly susceptible to substances that are known to reduce illusory percepts, like antipsychotic drugs. We thus quantified the changes in dorsal cortex activity associated with a single intraperitoneal injection of an antipsychotic drug (clozapine). In C57BL/6 mice that expressed GCaMP brain wide, we found that closed and open loop locomotion onsets were almost unaffected by clozapine (**Figures 4A and 4B**), while there was a small increase in open loop visual flow onset responses (**Figure 4C**). In mice that expressed GCaMP6 in Tlx3 positive L5 IT neurons, however, clozapine fundamentally changed both closed and open loop locomotion onset responses. In V1, both types of locomotion onset now resulted in a massive increase in activity (**Figures 4D and 4E**). Conversely, open loop visual flow onset responses remained largely unchanged (**Figure 4F**). These effects could not be explained by clozapine induced changes in hemodynamic occlusion (**Figure S5A**) or locomotion behavior (**Figures S5B and S5C**). Clozapine also had an opposing effect on the average correlation of activity with locomotion speed in Tlx3 positive L5 IT neurons. While the average correlation between activity and locomotion speed was increased in C57BL/6 mice that expressed GCaMP brain wide, the same measure was decreased in mice that expressed GCaMP6 in Tlx3 positive L5 IT neurons (**Figure S5D**). Finally, we confirmed that this effect was also present when recording somatic activity in V1. Using two-photon imaging, after clozapine administration we

230 observed an increase of somatic responses during locomotion onsets that was very similar to that
231 observed with widefield imaging (**Figures S5E and S5F**). Thus, consistent with the speculation that
232 Tlx3 positive L5 IT neurons might function as internal representation neurons, clozapine exhibited a
233 substantially stronger influence on locomotion onset responses in Tlx3 positive L5 IT neurons than
234 would be expected from the effect of clozapine on brain wide responses.

235 **Antipsychotic drugs decouple long-range cortico-cortical activity**

236 L5 IT neurons are likely the primary source of long-range cortical communication (Chen et al., 2019;
237 Harris et al., 2019; Leinweber et al., 2017). Given that clozapine increased locomotion onset
238 responses in L5 IT neurons in V1, we wondered whether clozapine might more generally change the
239 long-range influence between L5 IT neurons. To investigate this possibility, we computed the
240 correlations of calcium activity between the six regions of interest across both hemispheres and all
241 recording conditions. We did this first in C57BL/6 mice that expressed GCaMP brain wide before
242 (**Figure 5A**) and after a single intraperitoneal injection of clozapine (**Figure 5B**). Overall, clozapine
243 resulted in a relatively modest decrease in correlations. On repeating this experiment in mice that
244 expressed GCaMP6 in Tlx3 positive L5 IT neurons, we found a larger decrease in correlations that
245 appeared to be stronger for regions that were further apart (**Figures 5C and 5D**). To quantify these
246 changes, we plotted the correlations as a function of linear distance between the regions as
247 measured in a top-down view of dorsal cortex (**Figure S6A**). Note, this is only an approximation of
248 the actual axonal path length between the regions. To visualize the distribution of correlations, we
249 interpolated the data and represented them as heatmaps (**Figure S6B**). The resulting representation
250 for the data from C57BL/6 mice that expressed GCaMP brain wide before and after clozapine
251 injection is shown in **Figures 6A** and **6B**, respectively. We then split the data into approximately
252 equal portions of short- and long-range correlations using a cutoff of 0.9 times the bregma-lambda
253 distance (approximately 3.8 mm). While both short- and long-range correlations were reduced, this
254 reduction was not significant in either case (**Figure 6C**). We also found no evidence of a difference
255 between short- and long-range correlation changes. In mice that expressed GCaMP6 in Tlx3 positive
256 L5 IT neurons, however, we found a significant reduction in both short- and long-range correlations
257 (**Figures 6D and 6E**), and both were more strongly reduced than in C57BL/6 mice that expressed
258 GCaMP brain wide (C57BL/6 vs Tlx3-Cre x Ai148, short-range: $p < 0.05$; long-range: $p < 10^{-5}$; rank-sum
259 test). Moreover, the reduction in activity correlations was stronger for long-range correlations than
260 it was for short-range correlations (**Figure 6F**). To control for possible clozapine induced changes in
261 hemodynamic occlusion, we repeated the experiment and analyses in Tlx3-Cre mice that expressed
262 eGFP in L5 IT neurons and found that alterations in hemodynamic occlusion could not account for

263 the decrease in correlations but resulted in a small increase of the same metric (**Figure S6C-S6E**). To
264 further dissect the spatial scale at which this decorrelation occurs, we repeated the experiments in
265 Tlx3-Cre x Ai148 mice that expressed GCaMP6 in L5 IT neurons, recording calcium activity using both
266 a widefield and a two-photon microscope. We found that while the activity correlations measured
267 with the widefield imaging decreased (**Figure S7A-S7C**), pairwise somatic activity correlations
268 measured by two-photon imaging did not (**Figure S7D**). This is consistent with the idea that the
269 decorrelation primarily occurs for long-range interactions. Finally, to confirm that the clozapine
270 induced reduction in correlation was stronger in deep cortical layers, we repeated the experiment in
271 a population of L2/3 and L4 excitatory neurons using Cux2-CreERT2 x Ai148 mice. We found that
272 clozapine also decreased correlations of cortical activity in superficial excitatory neurons (**Figure S8**).
273 However, this reduction was significantly weaker than the reduction we observed in mice that
274 expressed GCaMP6 in Tlx3 positive L5 IT neurons (Cux2-CreERT2 x Ai148 vs Tlx3-Cre x Ai148, short-
275 range: $p < 0.005$, long-range: $p < 10^{-8}$, rank-sum test). Thus, administration of the antipsychotic drug
276 clozapine resulted in a decorrelation of activity across dorsal cortex that was stronger in L5 IT
277 neurons (Tlx3) than it was in either upper layer excitatory neurons (Cux2) or in the brain wide
278 average (C57BL/6).

279 To test whether the decorrelation of the activity of L5 IT neurons is specific to clozapine or might
280 more generally be a functional signature of antipsychotic drugs, we repeated the experiments with
281 two additional antipsychotic drugs, aripiprazole and haloperidol. We found that the principal effect
282 of decorrelation of the activity patterns of Tlx3 positive L5 IT neurons was preserved with both drugs
283 (**Figures 7A-7F**). These changes in correlation were absent upon injection of a psychostimulant,
284 amphetamine (**Figures 7G-7I**). Thus, it is possible that a decrease in long-range correlations between
285 cortical L5 IT neurons might be a common mechanism of action for antipsychotic drugs.

286 Changes in the correlation between cortical regions could either be driven by changes in correlated
287 external inputs or through changes in communication between cortical regions. If antipsychotic
288 drugs primarily reduce correlations by reducing the strength of communication between cortical
289 regions, independent of whether this communication is direct or indirect, we would expect to find
290 changes in the way responses spread between cortical regions. We used visuomotor prediction error
291 responses that originated in V1 (**Figure 3**) to quantify how the spread of these responses in Tlx3
292 positive L5 IT neurons was influenced by antipsychotic drugs. The computation of negative
293 prediction errors during movement is thought to be driven by an excitatory prediction of visual flow
294 mediated by long-range cortical input from L5 neurons in regions like A24b (Leinweber et al., 2017),
295 as well as an inhibitory bottom-up visual input. By contrast, the computation of a positive prediction

296 error during passive observation is thought to be driven by an excitatory bottom-up visual input and
297 an inhibitory top-down input. Thus, we would primarily expect to find a reduction in mismatch
298 responses in L5 IT neurons and a reduction in the spread of this signal to secondary visual regions.
299 This is indeed what we observed: Mismatch responses were partially reduced in V1 and almost
300 absent in V2am after injection of antipsychotic drugs (**Figure 8A**). While responses to onsets of
301 drifting gratings were also reduced in V2am, they were overall less affected by the antipsychotic
302 drugs than mismatch responses (**Figure 8B**). These results are consistent with the interpretation that
303 antipsychotic drugs reduce lateral communication in L5. Whether this communication is mediated by
304 direct long-range connections between L5 neurons, or indirectly via other cortical neurons or
305 subcortical loops, remains to be tested.

306 **DISCUSSION**

307 When interpreting our results, it should be kept in mind that the source of the widefield imaging
308 signal in these experiments is not entirely clear and is likely a combination of somatic, dendritic, and
309 axonal signals. Given that the signal attenuation half depth in cortex is on the order of 100 µm
310 (Aravanis et al., 2007), most signals likely come from the superficial 100 µm of tissue (Allen et al.,
311 2017). In the case of the Tlx3 recordings, this would mean that we were recording a mixture of
312 axonal and dendritic signals of the Tlx3 neurons that have their soma in L5 but have a dense net of
313 axons and dendrites in L1. In the case of the brain wide expression of GCaMP using an AAV-PHP.eB
314 in C57BL/6 mice, the signals we recorded likely also include contributions from thalamic axons. In
315 addition to this, there is a hemodynamic contribution to the signal (Allen et al., 2017; Ma et al.,
316 2016; Valley et al., 2020) that is the result of varying occlusion by blood vessels. We attempted to
317 correct for the hemodynamic response using a 405 nm wavelength isosbestic illumination of
318 GCaMP6 but could not recover the hemodynamic responses measured in eGFP experiments.
319 Accurate correction likely requires calibration on eGFP measurements (Valley et al., 2020). Given
320 that hemodynamic responses should not systematically differ between different mouse lines, and
321 that in the crystal skull preparation the contribution of hemodynamic occlusion to increases in
322 fluorescence was relatively small (**Figure S1**), these hemodynamic artefacts should not substantially
323 alter our conclusions. Lastly, it should be kept in mind that responses in these widefield recordings
324 inherently reflect population averages. Assuming there is some form of lateral inhibition among
325 neurons, population averages need not reflect responses of neurons that are tuned to the specific
326 stimulus presented. For example, the suppression to grating stimuli we observed in V1 Tlx3 positive
327 L5 IT neurons could be the result of a subset of Tlx3 neurons that are strongly responsive to the
328 specific grating presented suppressing the rest of the population of Tlx3 neurons. The sum of both

329 could then result in a net decrease in calcium activity. Thus, an understanding of the mechanism that
330 results in opposing population responses of Tlx3 positive L5 IT neurons to positive and negative
331 prediction errors will require measurements with single neuron resolution.

332 In our experiments we have focused on Tlx3 positive L5 IT neurons, but given that L5 IT neurons are
333 densely connected to L5 pyramidal tract neurons (Anderson et al., 2010; Kiritani et al., 2012) and to
334 L6 neurons (Xu et al., 2016; Yamawaki and Shepherd, 2015), it is not unlikely that these neuron types
335 would follow similar patterns of activity and exhibit similar susceptibility to the influence of
336 antipsychotic drugs. In the comparison of closed and open loop locomotion onsets, we do indeed
337 find that Ntsr1 positive L6 excitatory neurons exhibit similar levels of dissimilarity as those observed
338 in Tlx3 positive L5 IT neurons (**Figure 1L**). It is possible that responses in the Ntsr1 recordings,
339 however, were noisier than those in the Tlx3 recordings (**Figure S4**), likely because of the lower
340 dendritic and axonal volume of Ntsr1 positive neurons in L1. Thus, while we have focused on the
341 Tlx3 positive L5 IT neurons mainly for reasons of experimental convenience, it is possible that both
342 the differential activation in closed and open loop locomotion onsets as well as the susceptibility of
343 long-range correlations to antipsychotic drugs is a general feature of cortical layers 5 and 6.

344 It is still unclear what the relevant sites of action in the brain are of antipsychotic drugs.
345 Antipsychotic drugs are often antagonists of the D2 receptors, which are most strongly expressed in
346 striatum. Consequently, it is sometimes assumed that the relevant site of action of antipsychotics is
347 the striatum. Consistent with this, an increase in striatal dopamine activates auditory cortex (Maia
348 and Frank, 2017) and mediates hallucination-like perceptions in mice (Schmack et al., 2021). It is
349 intriguing, however, to speculate that the effects we observed in L5 IT neurons, which provide a
350 dominant input to striatum (Morita et al., 2019), may be an alternate site of action. While it is
351 possible that the primary site of action of the antipsychotic drugs with respect to the L5
352 decorrelation phenotype we observed is striatum, this is unlikely. Changes to striato-thalamo-
353 cortical loops could appear as changes in functional connectivity observed in cortex. However,
354 feedback from striatum to cortex is exclusively mediated through thalamus, and neither L4, the
355 primary thalamo-recipient layer in cortex, nor our brain wide recordings exhibited any of the effects
356 we saw in L5 IT neurons. Thus, the effects we saw in L5 IT neurons are either not inherited from
357 striatum or are mediated by a separate set of thalamic neurons via direct thalamic input to deep
358 cortical layers (Constantinople and Bruno, 2013; Douglas and Martin, 1991). Thalamocortical
359 collaterals in deep layers, however, come from thalamic neurons that project primarily to superficial
360 layers (Oberlaender et al., 2012). Thus, we think it is unlikely that the observed effects in L5 IT
361 neurons were inherited from striatum. Independent of whether the treatment-relevant site of action

362 of antipsychotic drugs is indeed in L5 IT neurons, the long-range decorrelation of activity we
363 observed after antipsychotic drug injection could be used as a basis for a functional screen for
364 compounds with antipsychotic efficacy. Given that in the brain wide recordings the decorrelation of
365 activity was weaker compared to that observed in Tlx3 positive L5 IT neurons, it might be possible to
366 test for similar effects in human subjects using layer specific fMRI recordings (Haarsma et al., 2020).

367 A rather surprising implication of our results is that the dominant mode of coupling in cortex might
368 be lateral, not vertical. Two findings would argue for this interpretation. First, while L5 was
369 differentially activated across cortical regions during closed and open loop locomotion onsets, L2/3
370 exhibited rather limited differences. Second, antipsychotics decorrelated L5 activity but had no
371 effect on L2/3. Both findings could be explained if the long-range lateral coupling within L5 is
372 stronger than the local vertical coupling between L2/3 and L5.

373 One of the diseases treated with antipsychotic drugs is schizophrenia. It has been speculated that
374 disrupted resting-state functional connectivity in brain networks involving cortex is central to the
375 pathogenesis of schizophrenia (Li et al., 2017; Northoff and Duncan, 2016). Treatment-naïve
376 schizophrenia patients predominantly exhibit increases in resting state functional connectivity
377 between cortical regions, while medicated schizophrenia patients exhibit more balanced fractions of
378 increased and decreased functional connections (Li et al., 2019). Auditory hallucinations, one of the
379 hallmark symptoms of schizophrenia, are associated with increased activation of diverse cortical
380 regions (Catafau et al., 1994; Dierks et al., 1999; Shergill et al., 2000). Thus, it is conceivable that
381 antipsychotic drugs counteract this by reducing the strength of long-range cortical connectivity
382 mediated by L5 IT neurons, independent of whether the increased activity in schizophrenic patients
383 is indeed driven by aberrant increases in the strength of long-range cortical connections or is a
384 consequence of an aberrant increase in the strength of striato-thalamo-cortical loops. However, a
385 direct involvement of cortical circuits in the pathogenesis of schizophrenia is consistent with the
386 glutamate hypothesis of schizophrenia. This hypothesis is based on the finding that NMDA receptor
387 antagonists induce schizophrenia-like symptoms (Moghaddam and Javitt, 2012), and that
388 disturbances of NMDA and AMPA receptor related gene expression are associated with
389 schizophrenia (Harrison and Weinberger, 2005; Singh et al., 2020). In V1, it has been shown that
390 NMDA receptors are necessary during visual development to establish normal prediction error
391 signaling (Widmer and Keller, 2021). Thus, it is conceivable that a disruption of glutamatergic
392 signaling in cortex that alters the way internal representations are activated by prediction errors is
393 central to the etiology of schizophrenia. If so, we should find impairments in all domains of cortical
394 function, including sensory processing. In the case of the sensory cortex, cortical dysfunctions should

be apparent earlier in development, concurrent with the critical period for plasticity in sensory areas of cortex. While the core symptoms of schizophrenia typically appear in late adolescence, sensory processing is indeed impaired in schizophrenic patients (Javitt, 2009) and is apparent, for example, in the reduction of surround suppression in V1 (Yoon et al., 2009). Interestingly, some of these disturbances are detectable already during childhood as visuo-perceptual and reading anomalies in some subjects that later develop schizophrenia (Parellada et al., 2017). Positive symptoms of schizophrenia can be explained in a predictive processing framework of cortical function as a disturbance of a prediction error based update of internal representations (Fletcher and Frith, 2009; Frith, 2005). There are two types of prediction error neurons, positive and negative, and, given that cortex likely implements a non-hierarchical variant of predictive processing (Garner and Keller, 2022), two types of internal representation neurons. One set of internal representation neurons is excited by positive prediction errors and inhibited by negative prediction errors, and the other one is inhibited by positive prediction errors and excited by negative prediction errors (Keller and Mrsic-Flogel, 2018). Tlx3 positive L5 IT neurons exhibited opposing responses to positive and negative prediction errors (**Figure 3**), consistent with the responses of internal representation neurons. Given that the effects of antipsychotic drugs are predominantly observed in L5 IT neurons, and that anesthesia is thought to decouple L5 neuron soma from their apical tuft and thereby prevent conscious perception (Suzuki and Larkum, 2020), we speculate that Tlx3 positive L5 IT neurons may be one type of internal representation neuron and one of the functionally relevant sites of antipsychotic action.

FIGURES

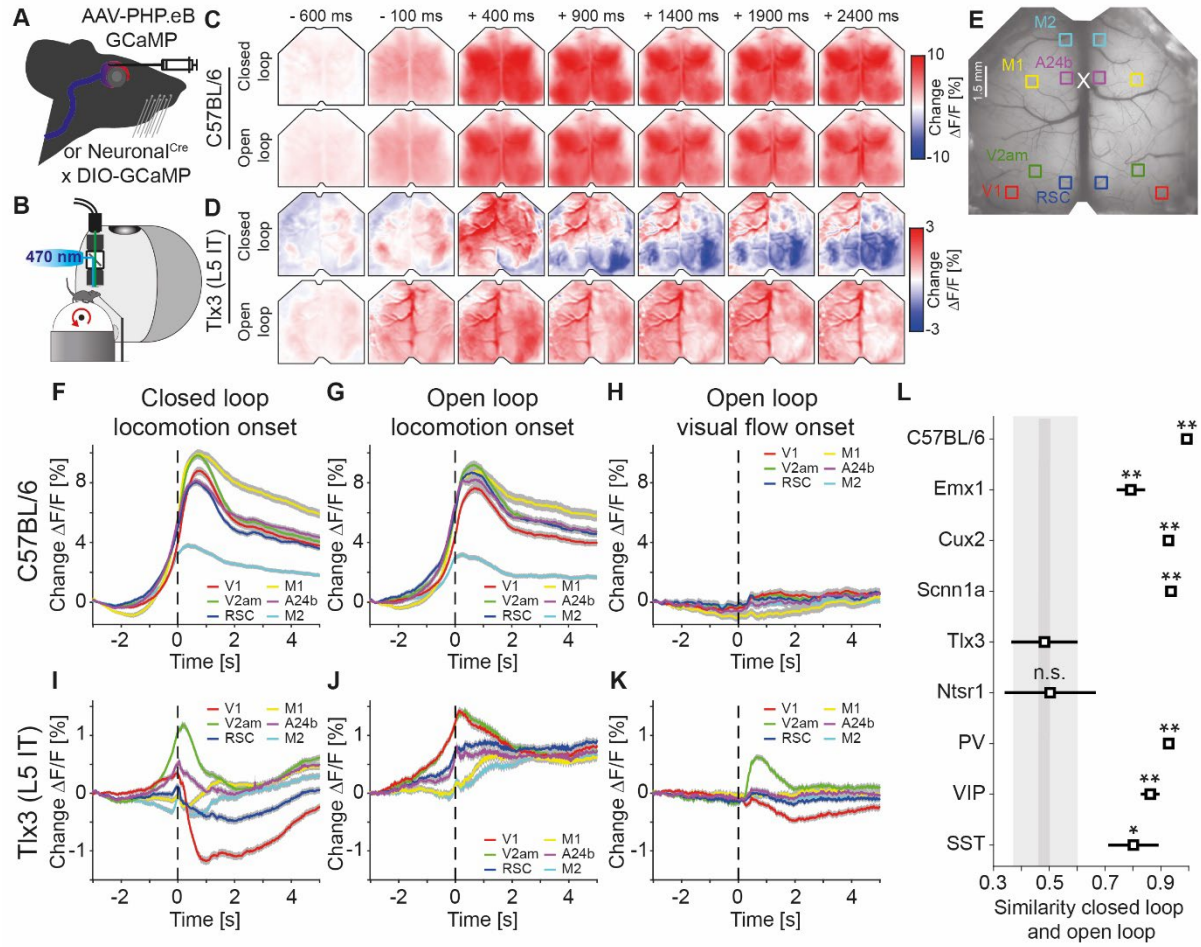

Figure 1. Activation patterns in deep cortical layers distinguished closed and open loop locomotion onsets more strongly than superficial layers.

(**A**) Schematic of GCaMP expression strategy. We either injected an AAV-PHP.eB virus retro-orbitally to express GCaMP brain wide (C57BL/6), in cortical excitatory neurons (Emx1-Cre) or in a subset of SST positive interneurons (see Methods and **Table S2**), or used the progeny of a cross of a cell type specific Cre driver line (Neuronal^{Cre}: Cux2-CreERT2, Scnn1a-Cre, Tlx3-Cre, Ntsr1-Cre, PV-Cre, VIP-Cre or SST-Cre) with the Ai148 GCaMP6 reporter line. All mice were then implanted with a crystal skull cranial window prior to imaging experiments.

(**B**) Schematic of the experimental setup. We imaged GCaMP fluorescence under 470 nm LED illumination with an sCMOS camera through a macroscope. Mice were free to locomote on an air supported spherical treadmill while coupled (closed loop), uncoupled (open loop), or no (dark) visual flow in the form of movement along a virtual corridor was displayed on a toroidal screen placed in front of the mouse. Walls of the virtual corridor were patterned with vertical sinusoidal gratings. In a separate condition, we then presented drifting grating stimuli (grating session, see Methods).

(**C**) Average response in an example C57BL/6 mouse that expressed GCaMP6 brain wide during closed loop locomotion onsets (top row, 83 onsets) and open loop locomotion onsets (bottom row, 153 onsets). Locomotion onsets in both conditions activated dorsal cortex similarly.

(**D**) As in **C**, but in an example Tlx3-Cre x Ai148 mouse that expressed GCaMP6 in L5 IT neurons during closed loop locomotion onsets (top row, 88 onsets) and open loop locomotion onsets (bottom row, 83 onsets). Note that activity decreased in posterior regions of dorsal cortex during closed loop locomotion onsets.

(**E**) Example crystal skull craniotomy marking the 6 regions of interest in each hemisphere we selected: primary visual cortex (V1, red), retrosplenial cortex (RSC, blue), antero-medial secondary visual cortex (V2am, green), primary motor cortex (M1, yellow), anterior cingulate cortex (A24b, purple), and secondary motor cortex (M2, cyan). The white cross marks bregma.

(**F**) Average response during closed loop locomotion onsets in C57BL/6 mice that expressed GCaMP brain wide in the 6 regions of interest (907 onsets in 6 mice, activity was averaged across corresponding regions in both hemispheres). Shading indicates SEM over onsets.

(**G**) As in **F**, but for open loop locomotion onsets (598 onsets in 6 mice).

(**H**) As in **F**, but for visual flow onsets in the open loop condition restricted to times when the mice were not locomoting (416 onsets in 6 mice).

(**I**) Average response during closed loop locomotion onsets in Tlx3-Cre x Ai148 mice that expressed GCaMP6 in L5 IT neurons (1919 onsets in 15 mice, activity was averaged across corresponding regions in both hemispheres). Shading indicates SEM over onsets.

(**J**) As in **I**, but for open loop locomotion onsets (1125 onsets in 15 mice).

(**K**) As in **J**, but for visual flow onsets during open loop sessions restricted to times when the mice were not locomoting (1189 onsets in 15 mice).

(**L**) Similarity of the average closed and open loop locomotion onset responses quantified as the correlation coefficient between the two in a window -5 s to +3 s around locomotion onset (see Methods). Error bars indicate SEM over the 12 (6 per hemisphere) cortical regions. Statistical comparisons are against the Tlx3 data: n.s.: not significant, *: $p < 0.05$, **: $p < 0.01$. See **Table S1** for all information on statistical testing.

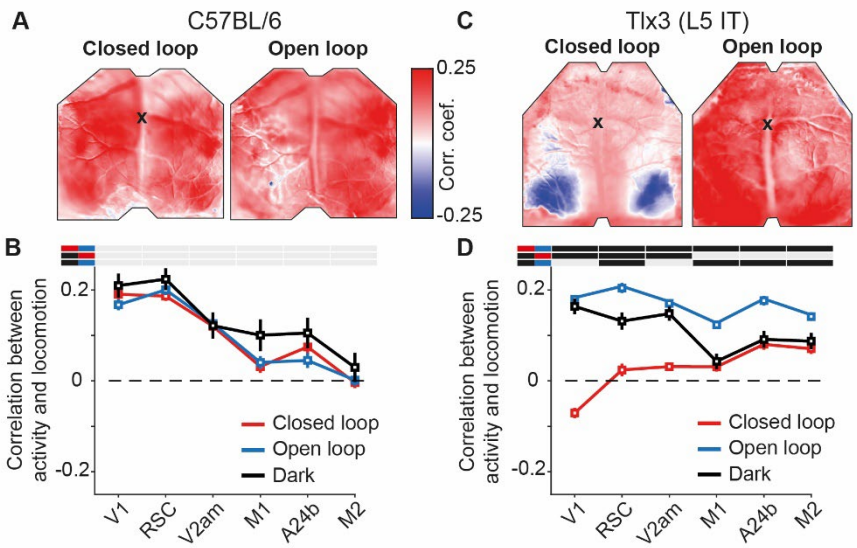

Figure 2. L5 IT neurons were differentially activated by locomotion depending on the type of visual feedback.

(**A**) Correlation between calcium activity and locomotion speed in the closed loop (left) and open loop (right) conditions, calculated for each pixel in the image for one example C57BL/6 mouse that expressed GCaMP brain wide. The black cross marks bregma. Activity in most of dorsal cortex correlates positively with locomotion speed in both closed and open loop conditions.

(**B**) Average correlation between calcium activity and locomotion speed in the 6 regions of interest in closed loop (red), open loop (blue) or dark (black) conditions in 6 C57BL/6 mice that expressed GCaMP brain wide (308, 316, and 68 5-minute sessions, respectively). Error bars indicate SEM over sessions. Bars above the plot indicate significant differences between conditions (compared conditions are indicated by colored line segments to the left, black: $p < 0.05$, gray: n.s., see **Table S1** for all information on statistical testing). On average, the correlation was highest in posterior dorsal cortex and was not different between conditions.

(**C**) As in **A**, but for an example Tlx3-Cre x Ai148 mouse that expressed GCaMP6 in L5 IT neurons. Correlations of calcium activity and locomotion speed were lower in the closed loop condition compared to the open loop condition, most prominently in posterior regions of dorsal cortex.

(**D**) As in **B**, but for 15 Tlx3-Cre x Ai148 mice that expressed GCaMP6 in L5 IT neurons (data from 420 closed loop, 394 open loop and 194 dark 5-minute sessions). Error bars indicate SEM over sessions. Correlation differed significantly between the closed and the open loop condition and was lowest in posterior dorsal cortex during the closed loop condition.

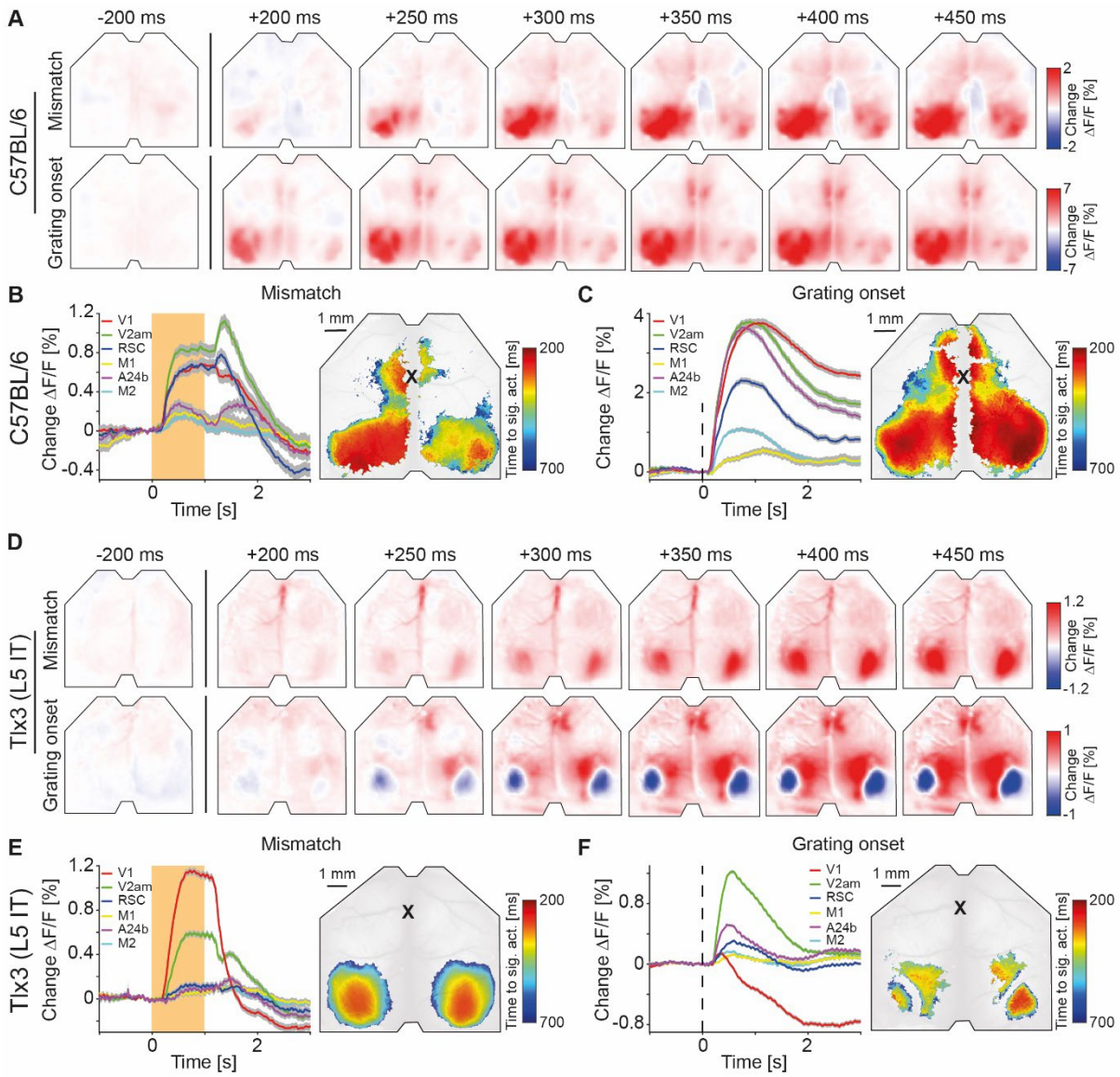

481

482 **Figure 3. Visuomotor prediction error responses in dorsal cortex originated in V1 and activated L5**
483 **IT neurons differentially.**

484 (**A**) Average responses to mismatches (top row, 230 onsets) and drifting gratings (bottom row, 86
485 onsets) in an example C57BL/6 mouse that expressed GCaMP brain wide.

486 (**B**) Left: Average response to mismatches in C57BL/6 mice that expressed GCaMP brain wide (2512
487 onsets in 6 mice, activity was averaged across corresponding regions in both hemispheres). Shading
488 indicates SEM over onsets. Orange shading indicates duration of mismatch event. Right: Average
489 time to significant activation to mismatch in 6 C57BL/6 mice (see Methods), overlayed onto an
490 example image of a craniotomy. Black cross marks bregma.

491 (**C**) As in **B**, but for drifting grating responses (1858 onsets in 6 mice).

492 (**D**) As in **A**, but in an example Tlx3-Cre x Ai148 mouse that expressed GCaMP6 in L5 IT neurons (top
493 row: mismatch, 292 onsets; bottom row: drifting gratings, 171 onsets).

(**E**) As in **B**, but for Tlx3-Cre x Ai148 mice that expressed GCaMP6 in L5 IT neurons (3297 onsets in 15 mice).

(**F**) As in **C**, but for Tlx3-Cre x Ai148 mice that expressed GCaMP6 in L5 IT neurons (5318 onsets in 15 mice).

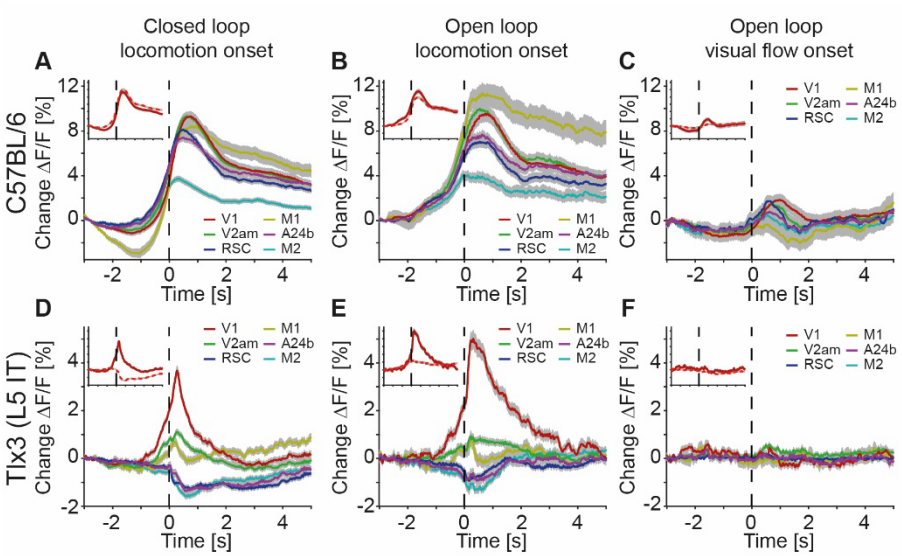

Figure 4. Clozapine increased locomotion related responses in L5 IT neurons in V1.

(**A**) Average response during closed loop locomotion onsets in C57BL/6 mice that expressed GCaMP brain wide (273 onsets in 4 mice, activity was averaged across corresponding regions in both hemispheres) after a single injection of the antipsychotic drug clozapine (see Methods). Shading indicates SEM over onsets. Inset: Comparison of responses for V1 in 4 naive C57BL/6 mice (dashed red, 720 onsets) and the same 4 mice after clozapine injection (dark red, same data as in main panel).

(**B**) As in **A**, but for open loop locomotion onsets after a clozapine injection (145 onsets in 4 mice; inset: 570 onsets in the same 4 mice before injection).

(**C**) As in **A**, but for open loop visual flow onsets restricted to times when the mice were not locomoting (99 onsets in 4 mice; inset: 404 onsets in the same 4 mice before injection).

(**D**) Average response during closed loop locomotion onsets in Tlx3-Cre x Ai148 mice that expressed GCaMP6 in layer L5 IT neurons (707 onsets in 5 mice, activity was averaged across corresponding regions in both hemispheres) after a single injection of the antipsychotic drug clozapine (see Methods). Shading indicates SEM over onsets. Inset: Comparison of responses for V1 in 5 naive Tlx3-Cre x Ai148 mice (dashed red, 1101 onsets) and the same 5 mice after clozapine injection (dark red, same data as in main panel).

(**E**) As in **D**, but for open loop locomotion onsets (350 onsets in 5 mice; inset: 348 onsets in the same 5 mice before injection).

(**F**) As in **D**, but for open loop visual flow onsets restricted to times when the mice were not locomoting (514 onsets in 5 mice; inset: 568 onsets in the same 5 mice before clozapine injection).

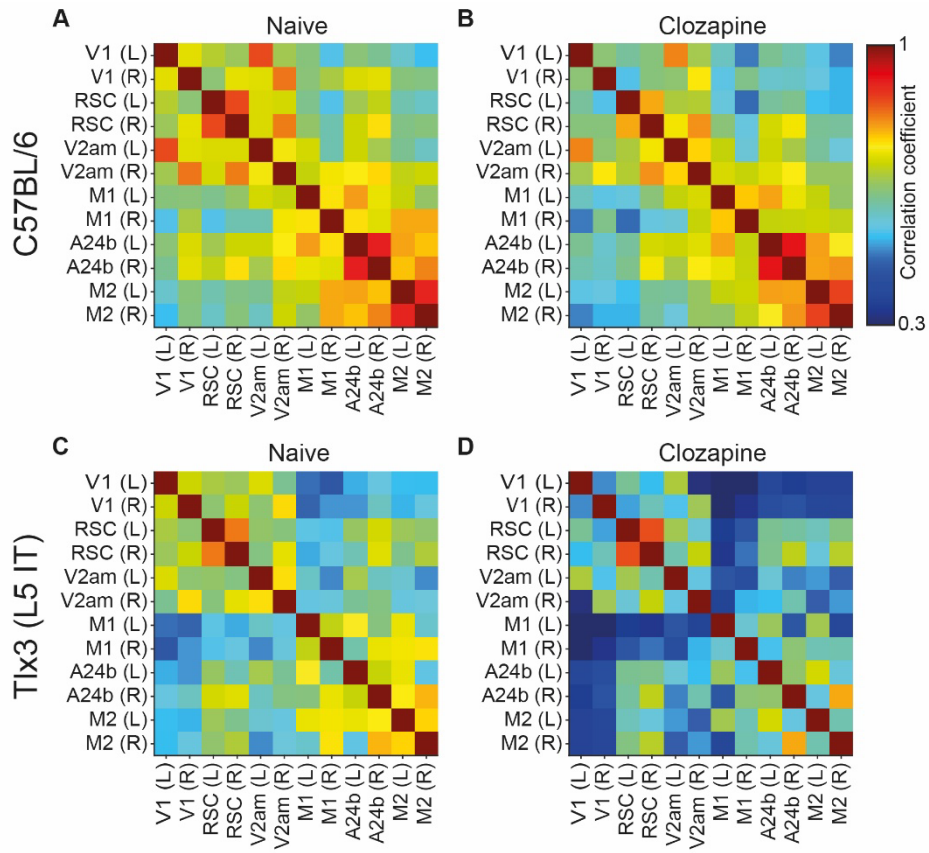

522

523 **Figure 5. Clozapine reduced activity correlations in dorsal cortex predominantly in L5 IT neurons.**

524 (**A**) Average correlation of activity between the 12 regions of interest in 4 C57BL/6 mice that
525 expressed GCaMP brain wide.

526 (**B**) As in **A**, but after a single injection of the antipsychotic drug clozapine in the same 4 C57BL/6
527 mice.

528 (**C**) Average correlation of activity between the 12 regions of interest in 5 Tlx3-Cre x Ai148 mice that
529 expressed GCaMP6 in layer L5 IT neurons.

530 (**D**) As in **C**, but after a single injection of the antipsychotic drug clozapine in the same 5 Tlx3-Cre x
531 Ai148 mice.

532

533

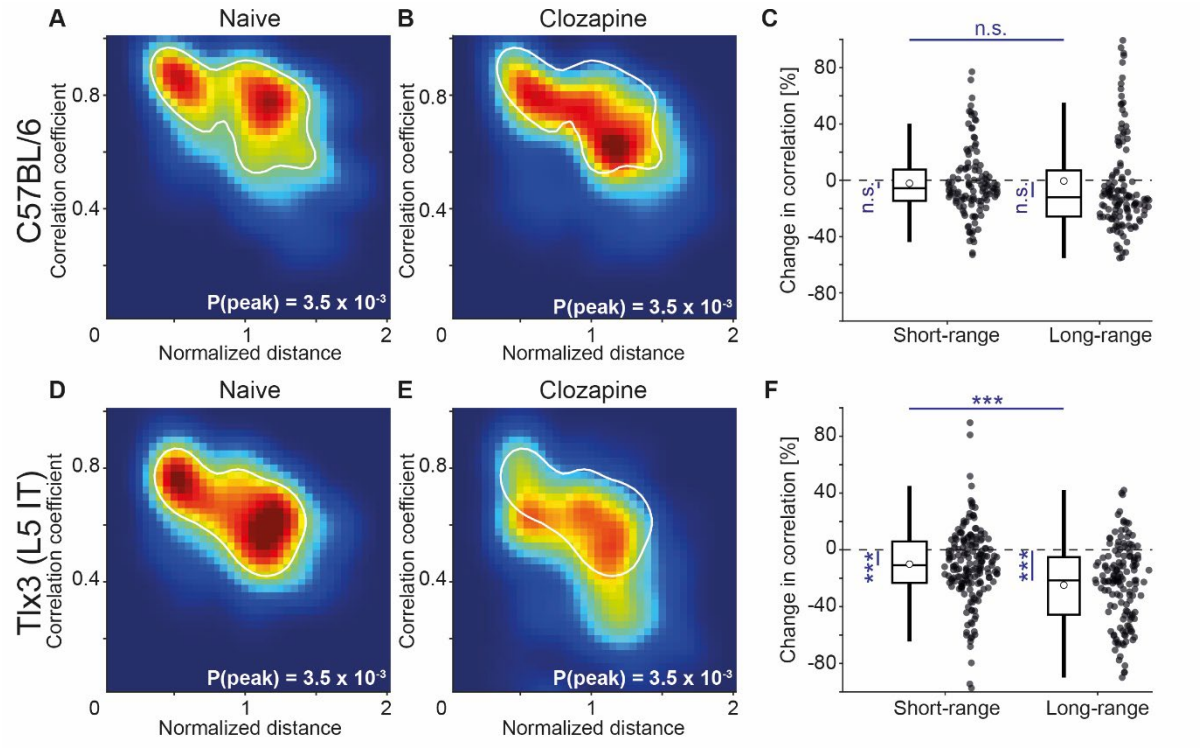

534

535 **Figure 6. L5 IT neurons exhibited the strongest clozapine induced reduction of long-range**
536 **correlations.**

537 (**A**) Density map of correlation coefficients as a function of distance between the regions, normalized
538 across mice by the bregma-lambda distance (see **Figure S6A and S6B**, and Methods), for 4 naive
539 C57BL/6 mice that expressed GCaMP brain wide. Peak density is indicated at the bottom right of the
540 plot and corresponds to the maximum value of the color scale (dark red). The white line is a contour
541 line drawn at 50% of peak value.

542 (**B**) As in **A**, but for the same 4 C57BL/6 mice after a single injection of the antipsychotic drug
543 clozapine. The white line is the contour line from panel **A** for comparison.

544 (**C**) Clozapine induced change in the activity correlation between regions, normalized to the
545 correlation coefficient in the naive state, in 4 C57BL/6 mice. Data were split into short- and long-
546 range activity correlations (see Methods). Boxes represent the median and the interquartile range.
547 The open circle indicates the mean of the distribution. The whiskers mark 1.5 times the interquartile
548 range. Dots are the individual data points (short-range: 122 pairs, long-range: 142 pairs). n.s.: not
549 significant. See **Table S1** for all information on statistical testing.

550 (**D**) As in **A**, but for 5 Tlx3-Cre x Ai148 mice that expressed GCaMP6 in L5 IT neurons.

551 (**E**) As in **B**, but for 5 Tlx3-Cre x Ai148 mice that expressed GCaMP6 in L5 IT neurons. The white line is
552 the contour line from panel **D** for comparison.

553 (**F**) As in **C**, but for 5 Tlx3-Cre x Ai148 mice that expressed GCaMP6 in L5 IT neurons (short-range: 182
554 pairs, long-range: 148 pairs). ***: $p < 0.001$.

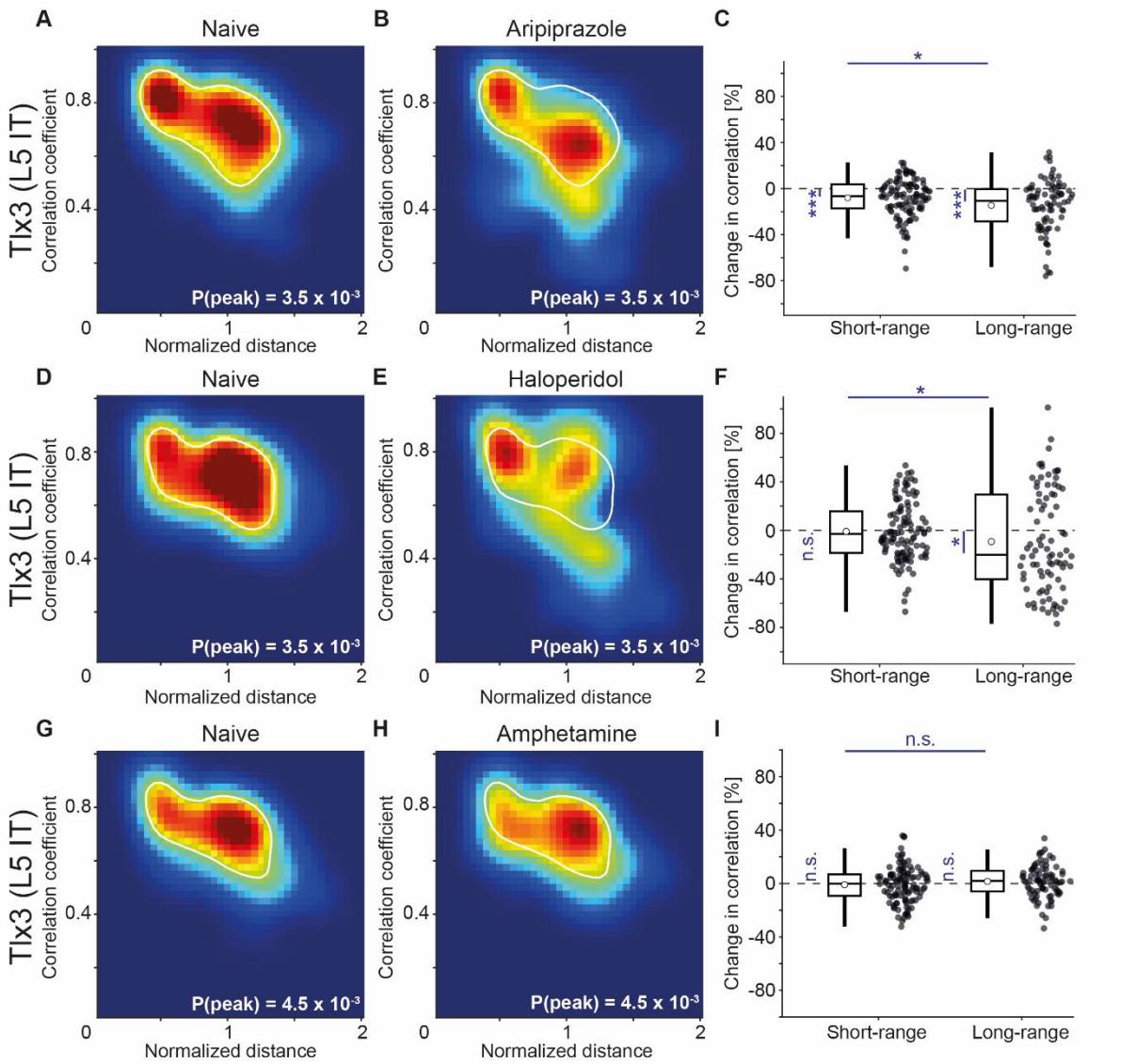

Figure 7. Antipsychotic drugs aripiprazole and haloperidol mimicked the decorrelation of L5 IT activity observed with clozapine while psychostimulant amphetamine did not.

(**A**) Density map of correlation coefficients as a function of distance between the regions, normalized across mice by the bregma-lambda distance (see **Figure S6A and S6B**, and Methods), for 3 Tlx3-Cre x Ai148 mice that expressed GCaMP6 in L5 IT neurons. Peak density is indicated at the bottom right of the plot and corresponds to the maximum value of the color scale (dark red). The white line is a contour line drawn at 50% of peak value.

(**B**) As in **A**, for the same 3 Tlx3-Cre x Ai148 mice, but after a single injection of the antipsychotic drug aripiprazole. The white line is the contour line from panel **A** for comparison.

(**C**) Aripiprazole induced change in the activity correlation between regions, normalized to the correlation coefficient in the naive state, in 3 Tlx3-Cre x Ai148 mice. Data were split into short- and long-range activity correlations (see Methods). Boxes represent the median and the interquartile range. The open circle indicates the mean of the distribution. The whiskers mark 1.5 times the

interquartile range. Dots are the individual data points (short-range: 114 pairs, long-range: 84 pairs). *: $p < 0.05$, ***: $p < 0.001$. See **Table S1** for all information on statistical testing.

(**D**) As in **A**, but for 3 different Tlx3-Cre x Ai148 mice.

(**E**) As in **D**, for the same 3 Tlx3-Cre x Ai148 mice, but after a single injection of the antipsychotic drug haloperidol. The white line is the contour line from panel **D** for comparison.

(**F**) As in **C**, but for the 3 mice that had received a single injection of the antipsychotic drug haloperidol (short-range: 114 pairs, long-range: 84 pairs). *: $p < 0.05$; n.s.: not significant.

(**G**) As in **A**, but for 3 different Tlx3-Cre x Ai148 mice.

(**H**) As in **G**, for the same 3 Tlx3-Cre x Ai148 mice, but after a single injection of the psychostimulant amphetamine. The white line is the contour line from panel **G** for comparison.

(**I**) As in **D**, but for the 3 mice that had received a single injection of the psychostimulant amphetamine (short-range: 114 pairs, long-range: 84 pairs). n.s.: not significant.

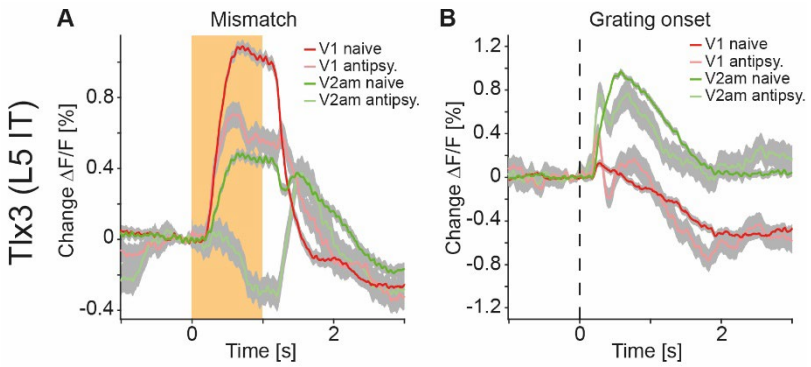

Figure 8. Antipsychotic drug treatment reduced responses to and propagation of negative prediction errors.

(**A**) Average responses to mismatches in Tlx3-Cre x Ai148 mice that expressed GCaMP6 in L5 IT neurons before (red: V1 naive, green: V2am naive, activity was averaged across corresponding regions in both hemispheres) and after (pale red: V1, pale green: V2am) injection of a single dose of an antipsychotic drug (data were averaged over all antipsychotics used: Clozapine: 5 mice, aripiprazole: 3 mice, and haloperidol: 3 mice). Orange shading indicates duration of the mismatch event. Gray shading indicates SEM over onsets (naive: 2464 onsets, antipsychotics: 2017 onsets).

(**B**) As in **A**, but for drifting grating onsets (naive: 3942 onsets, antipsychotics: 1645 onsets).

SUPPLEMENTAL FIGURES

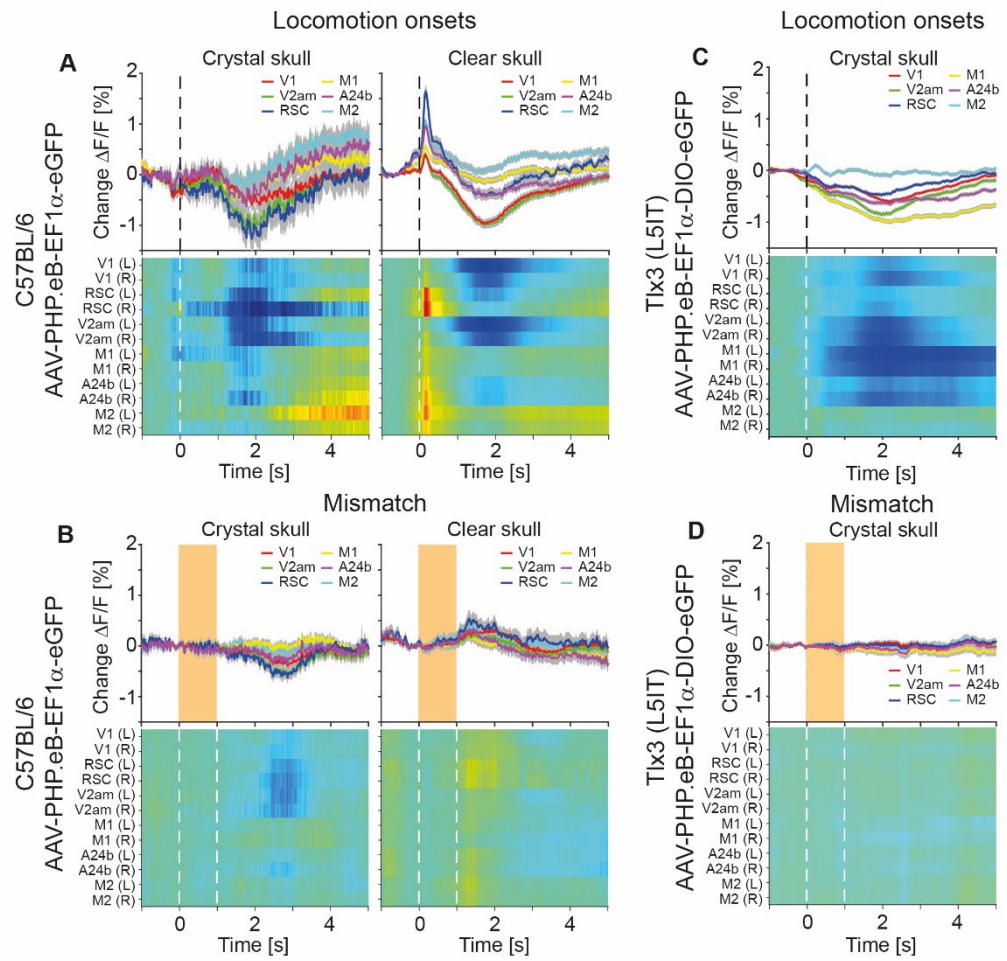

Figure S1. Fluorescence changes driven by hemodynamic occlusion. Related to Figure 1.

(**A**) Average responses during locomotion onsets in C57BL/6 mice that expressed eGFP brain wide using a crystal skull preparation (left: 3 mice, 96 locomotion onsets) or in similarly transfected mice using a clear skull preparation (right: 5 mice, 615 locomotion onsets) (see Methods). Top row shows the average activity of corresponding regions in dorsal cortex. Shading indicates SEM over onsets. The heatmaps in the bottom row show the responses for individual regions of interest. Heatmaps are scaled to the y-axis limits of the plot above (blue low, red high). Note, the fast onset transient apparent in the clear skull preparation was absent in the crystal skull preparation, while the slow decrease of activity was present in both. The increase in fluorescence at locomotion onset, which was primarily apparent in the clear skull preparation, is driven by hemodynamic occlusion.

(**B**) As in **A**, but for mismatches (left: 229 onsets in 3 mice, right: 228 onsets in 5 mice). Orange shading (top) or white dashed lines (bottom) indicate the duration of the mismatch stimulus.

(**C**) As in **A**, left, but for 7 Tlx3-Cre that had been retro-orbitally injected with an AAV-PHP.eB-DIO-eGFP to express eGFP in L5 IT neurons (1880 onsets).

609 (**D**) As in **B**, left, but for 7 Tlx3-Cre that had been retro-orbitally injected with an AAV-PHP.eB-DIO-
610 eGFP to express eGFP in L5 IT neurons (451 onsets).

611

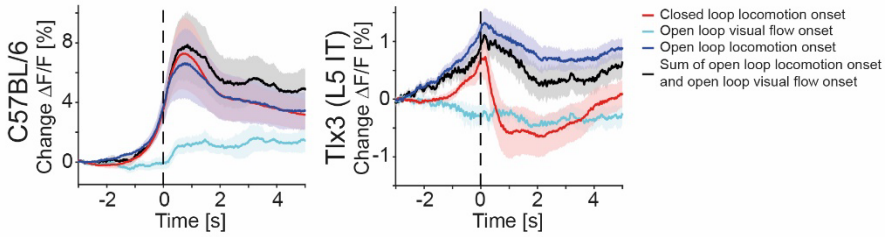

Figure S2. In V1, the sum of locomotion and visual flow onset could not explain the closed loop locomotion onset response of L5 IT neurons. Related to Figure 1.

Average responses during closed (red) and open loop (blue) locomotion onsets, as well as open loop visual flow (turquoise) onsets, and the sum of open loop locomotion and open loop visual flow onsets (black). In C57BL/6 mice that expressed GCaMP brain wide (left, 6 mice), closed loop locomotion onset responses in V1 were larger than open loop locomotion onset responses, and part of this difference could be explained by the visual flow onset responses. In Tlx3-Cre x Ai148 that expressed GCaMP6 in L5 IT neurons (right, 15 mice), closed loop locomotion onset responses in V1 cannot be explained as the sum of open loop locomotion and visual flow onset. Shading indicates SEM over mice.

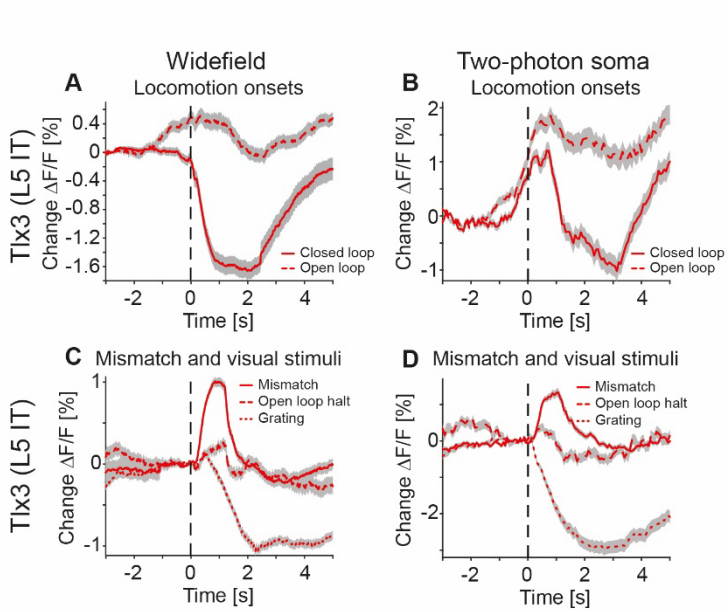

Figure S3. L5 IT soma recorded in V1 with two-photon imaging show similar patterns of activity as the widefield signal recorded at the surface of the dorsal cortex. Related to Figure 1.

(**A**) Average response of V1 recorded with the widefield macroscope during closed (solid, 1012 onsets) or open loop (dashed, 678 onsets) locomotion onsets in 7 Tlx3-Cre x Ai148 mice that expressed GCaMP6 in L5 IT neurons.

(**B**) Average response of L5 soma in V1, recorded with two-photon imaging in the same 7 Tlx3-Cre x Ai148 mice that expressed GCaMP6 in L5 IT neurons as in **A**, during either closed loop (solid) or open loop (dashed) locomotion onsets. Shading indicates SEM over 8434 neurons.

(**C**) As in **A**, but for responses to mismatches (solid, 1038 onsets), open loop halts (dashed, 410 onsets) or drifting grating onsets (dotted, 2014 onsets). Shading indicates SEM over onsets.

(**D**) As in **B**, but for responses to mismatches (solid), open loop halts (dashed) or drifting grating onsets (dotted). Shading indicates SEM over 8434 neurons.

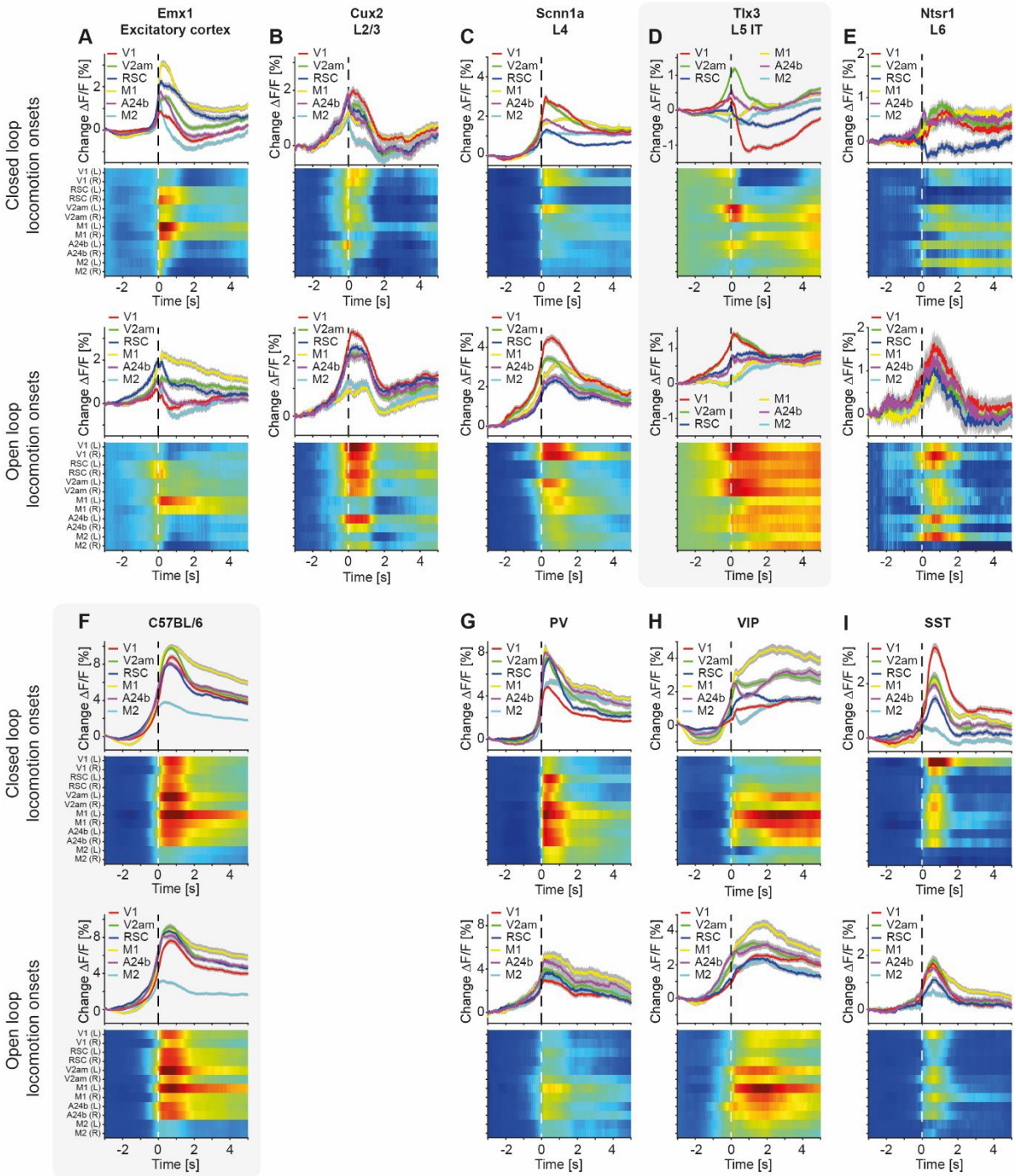

Figure S4. L5 IT neurons had strikingly different responses during closed and open loop locomotion onsets compared to other cortical neuron types. Related to Figure 1.

(**A**) Average response during closed loop locomotion onsets (top, 438 onsets) and open loop locomotion onsets (bottom, 286 onsets) in 4 Emx1-Cre mice that expressed GCaMP6 in excitatory cortical neurons. Shading indicates SEM over onsets. Heatmaps are scaled to the y-axis limits of the plot above (blue low, red high).

646 (**B**) As in **A**, but for 4 Cux2-CreERT2 x Ai148 mice that expressed GCaMP6 in upper layer excitatory
647 neurons (415 closed loop and 433 open loop locomotion onsets).

648 (**C**) As in **A**, but for 7 Scnn1a-Cre x Ai148 mice that expressed GCaMP6 in L4 excitatory neurons (839
649 closed loop and 313 open loop locomotion onsets).

650 (**D**) As in **A**, but for 15 Tlx3-Cre x Ai148 mice that expressed GCaMP6 specifically in L5 IT neurons
651 (1919 closed loop and 1125 open loop locomotion onsets). Data are the same as in **Figures 1I and**
652 **1K**.

653 (**E**) As in **A**, but for 3 Ntsr1-Cre x Ai148 mice that expressed GCaMP6 in excitatory L6 neurons (368
654 closed loop and 112 open loop locomotion onsets).

655 (**F**) As in **A**, but for 6 C57BL/6 mice that expressed GCaMP brain wide (907 closed loop and 598 open
656 loop locomotion onsets). Data are the same as in **Figures 1F and 1G**.

657 (**G**) As in **A**, but for 2 PV-Cre x Ai148 mice that expressed GCaMP6 in PV neurons (236 closed loop
658 and 110 open loop locomotion onsets).

659 (**H**) As in **A**, but for 6 VIP-Cre x Ai148 mice that expressed GCaMP6 in VIP neurons (618 closed loop
660 and 376 open loop locomotion onsets)

661 (**I**) As in **A**, but for 5 SST-Cre mice that expressed GCaMP6 in SST neurons (747 closed loop and 558
662 open loop locomotion onsets).

663

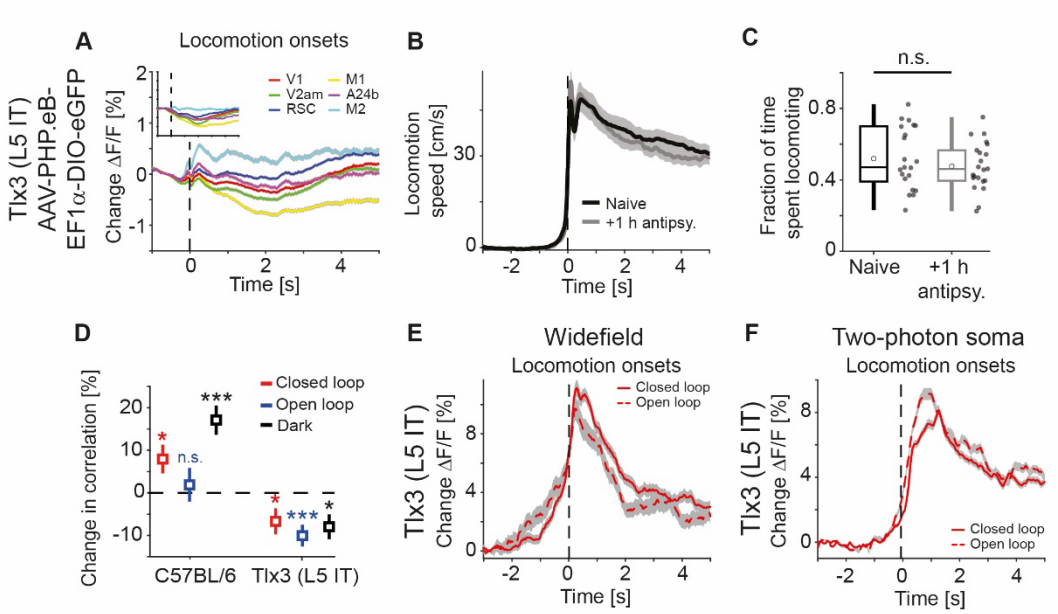

Figure S5. Additional information for antipsychotic drug data. Related to Figure 4.

(**A**) Average hemodynamic response during locomotion onsets in 7 Tlx3 mice that had been retro-orbitally injected with an AAV-PHP.eB-DIO-eGFP to express eGFP in L5 IT neurons (2331 onsets, responses were averaged across corresponding regions in both hemispheres) after a single injection of the antipsychotic drug clozapine (see Methods). Shading indicates SEM over onsets. Inset: Comparison of responses to locomotion onsets in the same mice before clozapine injection (same data as in **Figure S1C**, top panel).

(**B**) Average locomotion speed in 21 naive mice (black) and 22 mice that had been injected with either of the antipsychotic drugs clozapine, aripiprazole, or haloperidol (gray), for the data acquisition timepoint +1 h after injection. Shading indicates SEM over mice.

(**C**) Fraction of time spent locomoting above threshold (see Methods) for the 21 naive mice (black) and 22 mice that had been injected with either of the antipsychotic drugs clozapine, aripiprazole or haloperidol, for the data acquisition timepoint +1 h after injection (gray). Boxes represent the median and the interquartile range. The open circles indicate the mean of the distributions. The whiskers mark 1.5 times the interquartile range. Dots are the individual data points.

(**D**) Average correlation of activity and locomotion speed in dorsal cortex was increased after a single injection of the antipsychotic drug clozapine in 4 C57BL/6 mice that expressed GCaMP brain wide but decreased in 5 Tlx3-Cre x Ai148 mice that expressed GCaMP6 in L5 IT neurons, for all types of visual feedback. Error bars indicate SEM over mice and corresponding dorsal cortex regions (see Methods). n.s.: not significant, *: $p < 0.05$, ***: $p < 0.001$. See **Table S1** for all information on statistical testing.

(**E**) Average response of V1 recorded with the widefield macroscope during locomotion onsets in closed loop (solid, 376 onsets) or open loop (dashed, 245 onsets) in 3 Tlx3-Cre x Ai148 mice that

688 expressed GCaMP6 in L5 IT neurons and that had received an injection of the antipsychotic drug
689 clozapine. Shading indicates SEM over onsets.

690 (**F**) As in **E**, for the same 3 Tlx3 x Ai148 mice, but for responses recorded at L5 IT soma with two-
691 photon imaging. Shading indicates SEM over 5595 neurons.

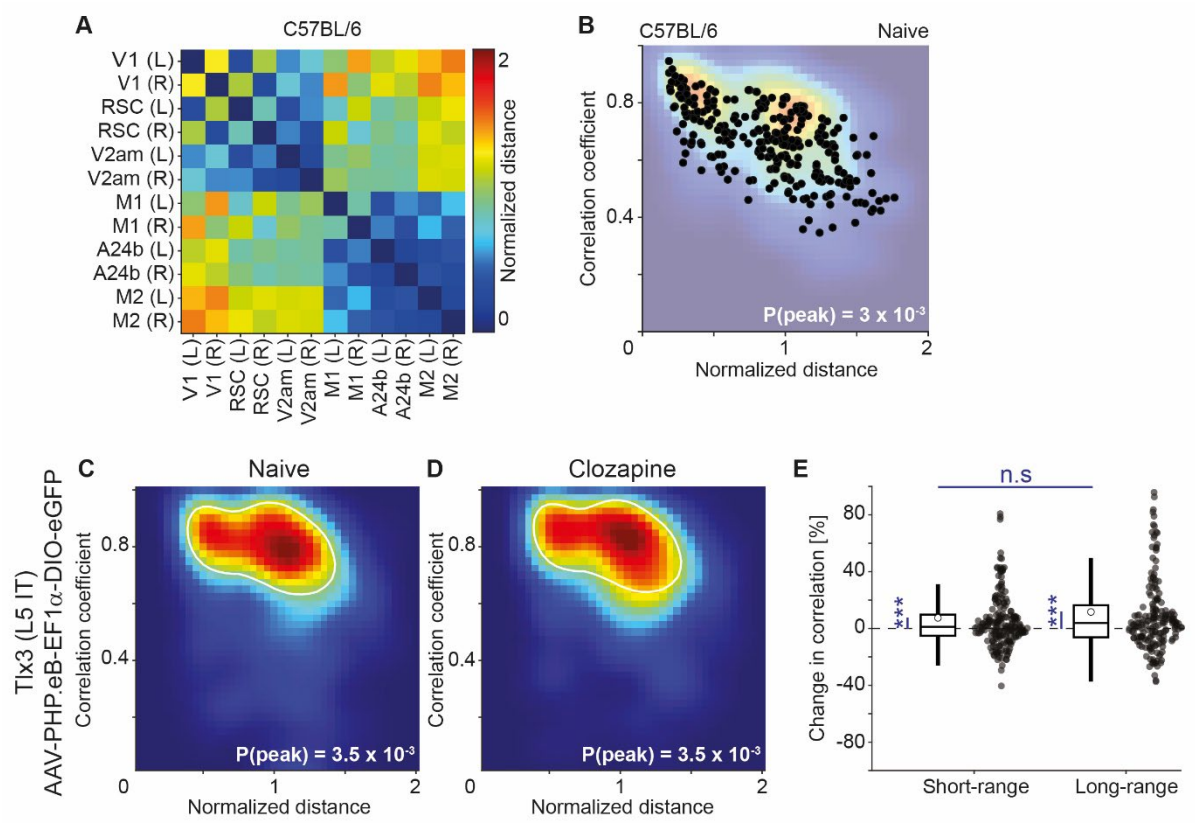

Figure S6. Calculation of the distance-correlation heatmaps. Related to Figure 5.

(**A**) For each pair of dorsal cortex regions, we calculated the distance between the regions in a top-down view of dorsal cortex, normalized by the distance between bregma and lambda for each mouse (data are from an example C57BL/6 mouse that expressed GCaMP6 brain wide).

(**B**) For each pair, we then plotted the activity correlation against this distance as calculated in **A** (black dots). We then interpolated this distribution using a 40-by-40 2D grid to obtain the density plots (faded background), shown for all mice and pairs in **Figures 6, 7, and S6-S8**.

(**C**) Density map of correlation coefficients as a function of distance between the regions, normalized across mice by the bregma-lambda distance (see panel **B** and Methods), for 6 Tlx3 mice that had been retro-orbitally injected with an AAV-PHP.eB-DIO-eGFP to express eGFP in L5 IT neurons. Peak density is indicated at the bottom right of the plot and corresponds to the maximum value of the color scale (dark red). The white line is a contour line drawn at 50% of peak value.

(**D**) As in **C**, but for the same 6 Tlx3-Cre mice that expressed eGFP in L5 IT neurons after a single injection of the antipsychotic drug clozapine. The white line is the contour from panel **C** for comparison.

(**E**) Clozapine induced change in the fluorescence correlation between regions, normalized to the correlation coefficient in the naive state, in 6 Tlx3-Cre mice that expressed eGFP in L5 IT neurons. Data were split into short- and long-range activity correlations (see Methods). Boxes represent the median and the interquartile range. The open circle indicates the mean of the distribution. The

whiskers mark 1.5 times the interquartile range. Dots are the individual data points (short-range: 204 pairs, long-range: 192 pairs). ***: $p < 0.001$, n.s.: not significant. See **Table S1** for all information on statistical testing.

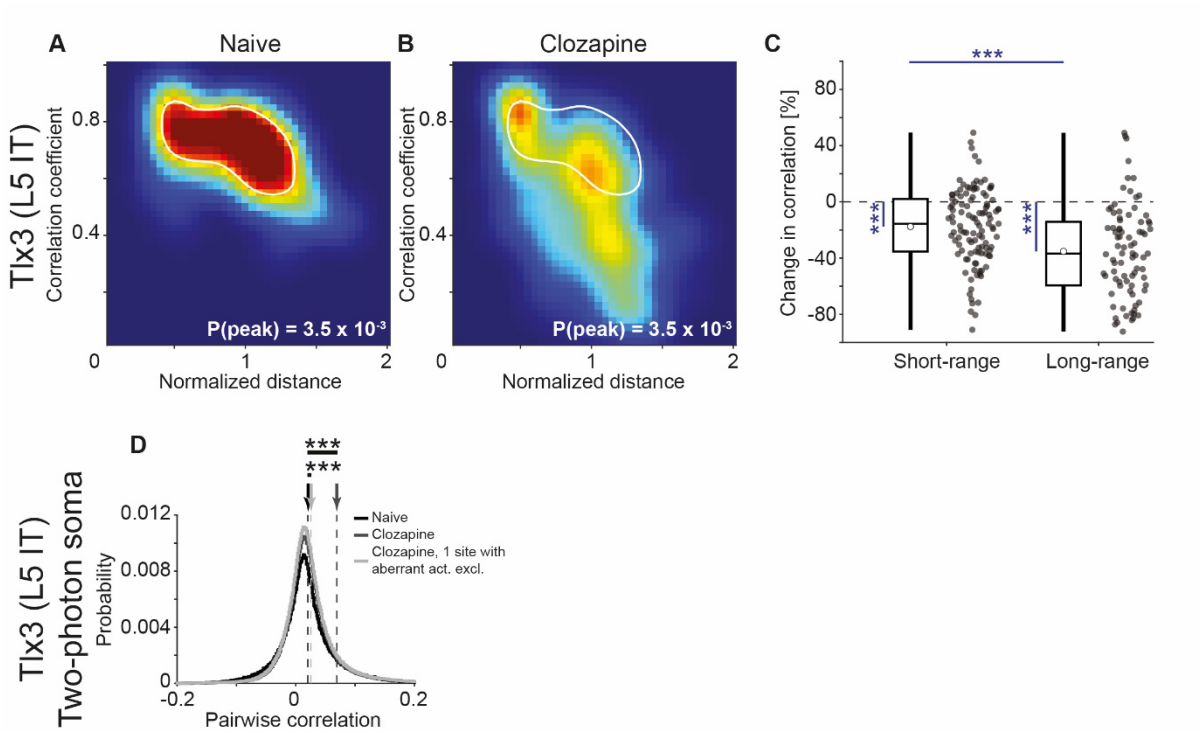

Figure S7. The clozapine induced decorrelation was not present in local somatic correlations. Related to Figure 6.

(**A**) Density map of correlation coefficients as a function of distance between the regions, normalized across mice by the bregma-lambda distance (see **Figures S6A and S6B**, and Methods), for 3 Tlx3-Cre x Ai148 mice that expressed GCaMP6 in L5 IT neurons. Peak density is indicated at the bottom right of the plot and corresponds to the maximum value of the color scale (dark red). The white line is a contour line drawn at 50% of peak value.

(**B**) As in **A**, but for the same 3 Tlx3-Cre x Ai148 mice after a single injection of the antipsychotic drug clozapine. The white line is the contour line from panel **A** for comparison.

(**C**) Clozapine induced change in the activity correlation between regions, normalized to the correlation coefficient in the naive state, in 3 Tlx3-Cre x Ai148 mice. Data were split into short- and long-range activity correlations (see Methods). Boxes represent the median and the interquartile range. The open circle indicates the mean of the distribution. The whiskers mark 1.5 times the interquartile range. Dots are the individual data points (short-range: 114 pairs, long-range: 84 pairs). ***, $p < 0.001$. See **Table S1** for all information on statistical testing.

(**D**) Distribution of pairwise neuronal activity correlations recorded with two-photon imaging at the L5 soma, in the same 3 Tlx3-Cre x Ai148 mice as in panels **A-C**, before (naive, black, 1991 neurons and 384108 pairs) and after injection of the antipsychotic drug clozapine (dark gray, 7863 neurons and 885596 pairs or pale gray, 1 field of view excluded, 7534 neurons and 831640 pairs). Dashed lines mark the mean of the respective distributions as indicated by the arrows on top. Note that after clozapine injection, we observed aberrantly high neuronal synchrony in 1 out of 25 recorded fields of view that substantially increased the average pairwise correlation as indicated by the two

740 curves that compare the clozapine data. In either comparison, clozapine significantly increased local
741 pairwise activity correlations.

742

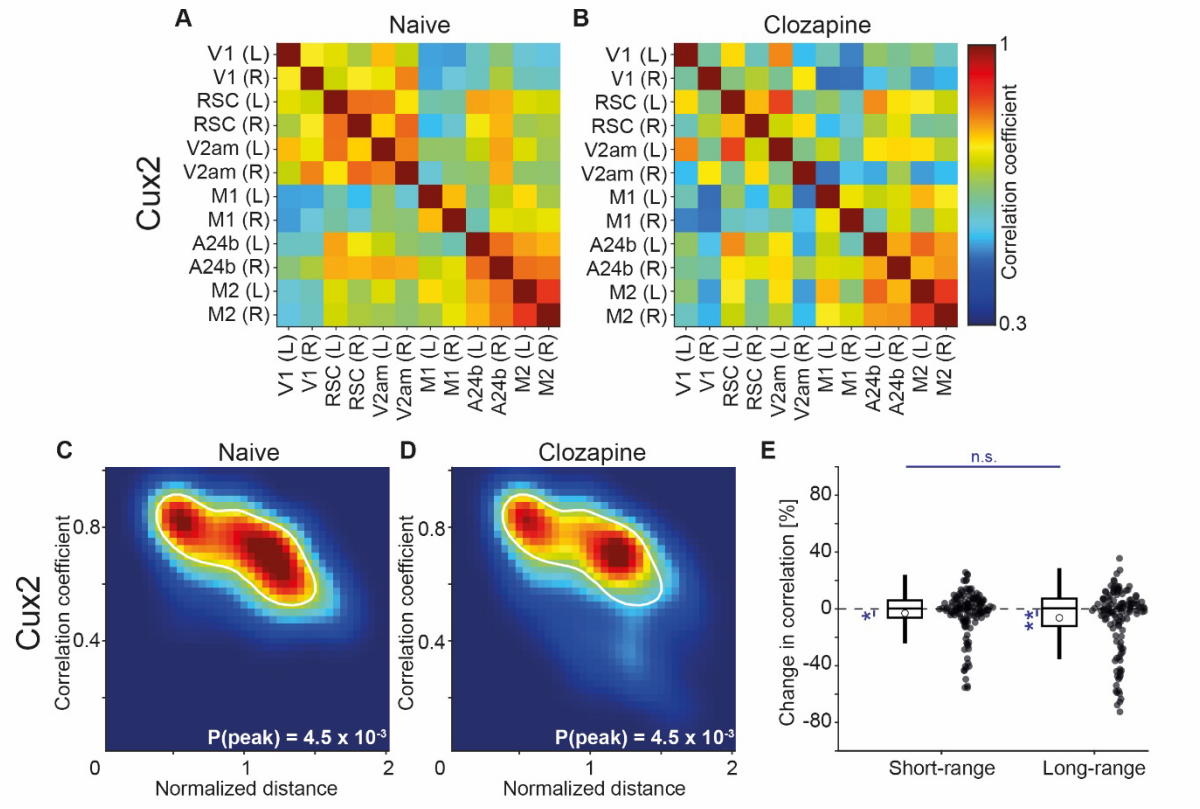

Figure S8. The clozapine induced decorrelation of dorsal cortex activity was weaker in superficial cortical layers than in L5. Related to Figure 6.

(**A**) Average correlation of activity between the 12 regions of interest in 4 Cux2-CreERT2 x Ai148 mice that expressed GCaMP6 in upper layer excitatory neurons.

(**B**) As in **A**, but for the same 4 Cux2-CreERT2 x Ai148 mice after a single injection of the antipsychotic drug clozapine.

(**C**) Density map of correlation coefficients as a function of distance between the regions, normalized across mice by the bregma-lambda distance (see **Figure S6A and S6B**, and Methods), for 4 naive Cux2-CreERT2 x Ai148 mice that expressed GCaMP6 in upper layer excitatory neurons. Peak density is indicated at the bottom right of the plot and corresponds to the maximum value of the color scale (dark red). The white line is a contour line drawn at 50% of peak value.

(**D**) As in **C**, but for the same 4 Cux2-CreERT2 x Ai148 mice after a single injection of the antipsychotic drug clozapine. The white line is the contour line from panel **C** for comparison.

(**E**) Clozapine induced change in the activity correlation between regions, normalized to the correlation coefficient in the naive state, in 4 Cux2-CreERT2 x Ai148 mice. Data were split into short- and long-range activity correlations (see Methods). Boxes represent the median and the interquartile range. The open circle indicates the mean of the distribution. The whiskers mark 1.5 times the interquartile range. Dots are the individual data points (short-range: 137 pairs, long-range: 127 pairs). n.s.: not significant, *: $p < 0.05$, **: $p < 0.01$. See **Table S1** for all information on statistical testing.

764 **SUPPLEMENTAL TABLES**

765 **Table S1. Statistical comparisons for bar and violin plots.**

Figure reference	Description (N_1 vs N_2)	Test	N_1 (mice)	N_2 (mice)	Unit	P-value
Figure 1L	Tlx3 vs C57BL/6	T-test	12 (15)	12 (6)	Regions	0.0012
	Tlx3 vs Emx1	T-test	12 (15)	12 (4)	Regions	0.0019
	Tlx3 vs Cux2	T-test	12 (15)	12 (4)	Regions	0.0045
	Tlx3 vs Scnn1a	T-test	12 (15)	12 (7)	Regions	0.0025
	Tlx3 vs Ntsr1	T-test	12 (15)	12 (3)	Regions	0.9175
	Tlx3 vs PV	T-test	12 (15)	12 (2)	Regions	0.0033
	Tlx3 vs VIP	T-test	12 (15)	12 (6)	Regions	0.0080
	Tlx3 vs SST	T-test	12 (15)	12 (5)	Regions	0.0384
Figure 2B	V1					
	Closed loop vs open loop	Rank-sum	308 (6)	316 (6)	Sessions	0.1088
	Closed loop vs dark	Rank-sum	308 (6)	68 (6)	Sessions	0.4131
	Open loop vs dark	Rank-sum	316 (6)	68 (6)	Sessions	0.1064
	RSC					
	Closed loop vs open loop	Rank-sum	308 (6)	316 (6)	Sessions	0.5522
	Closed loop vs dark	Rank-sum	308 (6)	68 (6)	Sessions	0.0786
	Open loop vs dark	Rank-sum	316 (6)	68 (6)	Sessions	0.2343
	V2am					
	Closed loop vs open loop	Rank-sum	308 (6)	316 (6)	Sessions	0.7924
	Closed loop vs dark	Rank-sum	308 (6)	68 (6)	Sessions	0.8326
	Open loop vs dark	Rank-sum	316 (6)	68 (6)	Sessions	0.9669
	M1					
	Closed loop vs open loop	Rank-sum	308 (6)	316 (6)	Sessions	0.9640
	Closed loop vs dark	Rank-sum	308 (6)	68 (6)	Sessions	0.0974
	Open loop vs dark	Rank-sum	316 (6)	68 (6)	Sessions	0.1597
	A24b					
	Closed loop vs open loop	Rank-sum	308 (6)	316 (6)	Sessions	0.1549
	Closed loop vs dark	Rank-sum	308 (6)	68 (6)	Sessions	0.4190
	Open loop vs dark	Rank-sum	316 (6)	68 (6)	Sessions	0.1540
	M2					
	Closed loop vs open loop	Rank-sum	308 (6)	316 (6)	Sessions	0.7265
	Closed loop vs dark	Rank-sum	308 (6)	68 (6)	Sessions	0.6720
	Open loop vs dark	Rank-sum	316 (6)	68 (6)	Sessions	0.6075
Figure 2D	V1					
	Closed loop vs open loop	Rank-sum	420 (15)	394 (15)	Sessions	$<10^{-10}$
	Closed loop vs dark	Rank-sum	420 (15)	194 (15)	Sessions	$<10^{-10}$
	Open loop vs dark	Rank-sum	394 (15)	194 (15)	Sessions	0.6851
	RSC					
	Closed loop vs open loop	Rank-sum	420 (15)	394 (15)	Sessions	$<10^{-10}$
	Closed loop vs dark	Rank-sum	420 (15)	194 (15)	Sessions	$<10^{-4}$
	Open loop vs dark	Rank-sum	394 (15)	194 (15)	Sessions	0.0010
	V2am					
	Closed loop vs open loop	Rank-sum	420 (15)	394 (15)	Sessions	$<10^{-10}$
	Closed loop vs dark	Rank-sum	420 (15)	194 (15)	Sessions	$<10^{-9}$
	Open loop vs dark	Rank-sum	394 (15)	194 (15)	Sessions	0.1570
	M1					
	Closed loop vs open loop	Rank-sum	420 (15)	394 (15)	Sessions	$<10^{-9}$
	Closed loop vs dark	Rank-sum	420 (15)	194 (15)	Sessions	0.5668
	Open loop vs dark	Rank-sum	394 (15)	194 (15)	Sessions	$<10^{-4}$

	A24b					
	Closed loop vs open loop	Rank-sum	420 (15)	394 (15)	Sessions	$<10^{-7}$
	Closed loop vs dark	Rank-sum	420 (15)	194 (15)	Sessions	0.6103
	Open loop vs dark	Rank-sum	394 (15)	194 (15)	Sessions	0.0001
	M2					
	Closed loop vs open loop	Rank-sum	420 (15)	394 (15)	Sessions	$<10^{-4}$
	Closed loop vs dark	Rank-sum	420 (15)	194 (15)	Sessions	0.5034
	Open loop vs dark	Rank-sum	394 (15)	194 (15)	Sessions	0.0111
Figure 6C	Short-range vs no change	T-test	122 (4)	-	Pairs	0.3791
	Long-range vs no change	T-test	142 (4)	-	Pairs	0.9035
	Short-range vs long-range	Rank-sum	122 (4)	142 (4)	Pairs	0.0511
Figure 6F	Short-range vs no change	T-test	182 (5)	-	Pairs	$<10^{-5}$
	Long-range vs no change	T-test	148 (5)	-	Pairs	$<10^{-10}$
	Short-range vs long-range	Rank-sum	182 (5)	148 (5)	Pairs	$<10^{-4}$
Figure 7C	Short-range vs no change	T-test	114 (3)	-	Pairs	$<10^{-5}$
	Long-range vs no change	T-test	84 (3)	-	Pairs	$<10^{-7}$
	Short-range vs long-range	Rank-sum	114 (3)	84 (3)	Pairs	0.0347
Figure 7F	Short-range vs no change	T-test	114 (3)	-	Pairs	0.7058
	Long-range vs no change	T-test	84 (3)	-	Pairs	0.0435
	Short-range vs long-range	Rank-sum	114 (3)	84 (3)	Pairs	0.0199
Figure 7I	Short-range vs no change	T-test	114 (3)	-	Pairs	0.4865
	Long-range vs no change	T-test	84 (3)	-	Pairs	0.2184
	Short-range vs long-range	Rank-sum	114 (3)	84 (3)	Pairs	0.1633
Figure S5C	Naive vs +1 h antipsy.	Rank-sum	21	22	Mice	0.4735
Figure S5D	C57BL/6					
	Closed loop vs no change	T-test	24 (4)	-	Regions	0.0277
	Open loop vs no change	T-test	24 (4)	-	Regions	0.6384
	Dark vs no change	T-test	24 (4)	-	Regions	$<10^{-4}$
	Tlx3					
	Closed loop vs no change	T-test	30 (5)	-	Regions	0.0365
	Open loop vs no change	T-test	30 (5)	-	Regions	0.0004
	Dark vs no change	T-test	30 (5)	-	Regions	0.0104
Figure S6E	Short-range vs no change	T-test	204 (7)	-	Pairs	0.0006
	Long-range vs no change	T-test	192 (7)	-	Pairs	$<10^{-4}$
	Short-range vs long-range	Rank-sum	204 (7)	192 (7)	Pairs	0.2540
Figure S7C	Short-range vs no change	T-test	114 (3)	-	Pairs	$<10^{-4}$
	Long-range vs no change	T-test	84 (3)	-	Pairs	$<10^{-4}$
	Short-range vs long-range	Rank-sum	114 (3)	84 (3)	Pairs	$<10^{-4}$
Figure S7D	Naive vs clozapine	Rank-sum	384108 (7)	885596	Pairs	$<10^{-4}$
	Naive vs clozapine 1 site excl.	Rank-sum	384108 (7)	831640	Pairs	$<10^{-4}$
Figure S8E	Short-range vs no change	T-test	137 (4)	-	Pairs	0.0262
	Long-range vs no change	T-test	127 (4)	-	Pairs	0.0019
	Short-range vs long-range	Rank-sum	137 (4)	127 (4)	Pairs	0.9537

768 **Table S2. Indicator expression strategy in individual mice.**

Nbr. mice	Genotype	Virus	Figures
3	C57BL/6	AAV-PHP.eB-hSyn1-jGCaMP7f	**1C, 1F-1H, 1L, 2A and 2B, 3A-3C, 4A-4C, 5A and 5B, 6A-6C, S2, S4F, S5B-S5D, S6A and S6B**
3	C57BL/6	AAV-PHP.eB-EF1α-GCaMP6s	**1F-1H, 1L, 2B, 3B and 3C, 4A-4C, 5A and 5B, 6A-6C, S2, S4, S5B-S5D**
8	C57BL/6	AAV-PHP.eB-EF1α-eGFP	**S1**
4	Emx1-Cre	AAV-PHP.eB-DIO-EF1α-GCaMP6s	**1L and S4A**
4	Cux2-CreERT2 x Ai148	-	**1L, S4B and S8**
7	Scnn1a-Cre x Ai148	-	**1L and S4C**
22	Tlx3-Cre x Ai148	-	**1D, 1I-1L, 2C and 2D, 3D-3F, 4D-4F, 5C and 5D, 6D-6F, 7, 8, S2, S3D, S4, S5B-S5F, S7**
7	Tlx3-Cre	AAV-PHP.eB-EF1α-DIO-eGFP	**S1C and S1D, S5A, S6C-S6E**
3	Ntsr1-Cre x Ai148	-	**1L and S4E**
2	PV-Cre x Ai148	-	**1L and S4G**
6	VIP-Cre x Ai148	-	**1L and S4H**
4	SST-Cre	AAV-PHP.eB-DIO-EF1α-jGCaMP7f	**1L and S4I**
1	SST-Cre x Ai148	-	**1L and S4I**

769

770 **METHODS**

771 **Key Resource Table**

REAGENT or RESOURCE	Source	Identifier
Bacterial and virus strains		
AAV-PHP.eB-hSyn1-jGCaMP7f (10^{13} GC/ml)	FMI vector core	vector.fmi.ch
AAV-PHP.eB-EF1α-GCaMP6s (10^{13} GC/ml)	FMI vector core	vector.fmi.ch
AAV-PHP.eB-DIO-EF1α-GCaMP6s (10^{13} GC/ml)	FMI vector core	vector.fmi.ch
AAV-PHP.eB-DIO-EF1α-jGCaMP7f (10^{12} GC/ml)	FMI vector core	vector.fmi.ch
AAV-PHP.eB-EF1α-eGFP (10^{13} GC/ml)	FMI vector core	vector.fmi.ch
AAV-PHP.eB-EF1α-DIO-eGFP (10^{15} GC/ml)	FMI vector core	vector.fmi.ch
Chemicals, peptides, and recombinant proteins		
Fentanyl citrate	Actavis	CAS 990-73-8
Midazolam (Dormicum)	Roche	CAS 59467-96-8
Medetomidine (Domitor)	Orion Pharma	CAS 86347-14-0
Ropivacaine	Presenius Kabi	CAS 132112-35-7
Lidocaine	Bichsel	CAS 137-58-6
Buprenorphine	Reckitt Benckiser Healthcare	CAS 52485-79-7
Ophthalmic gel (Humigel)	Virbac	N/A
Flumazenil (Anexate)	Roche	CAS 78755-81-4
Atipamezole (Antisedan)	Orion Pharma	CAS 104054-27-5
N-Butyl-2-cyanoacrylate (Histoacryl)	Braun	CAS 6606-65-1
Dental cement (Paladur)	Heraeus Kulzer	CAS 9066-86-8
Metacam	Boehringer Ingelheim	CAS 71125-39-8
Clozapine (powder)	Novartis	CAS 5786-21-0
Aripiprazole (intramuscular injection solution 7.5 mg/ml)	Otsuka Pharmaceutical	CAS 129722-12-9
Haloperidol (intramuscular injection solution 5 mg/ml)	Janssen	CAS 52-86-8
Amphetamine (powder)	Hänseler	CAS 60-13-9
Tamoxifen food	Envigo	CAS 10540-29-1 (TD.55125)
Deposited data		
All data and code used to generate manuscript figures	This paper	data.fmi.ch
Experimental models: Organisms/strains		
Mus musculus: C57BL/6	Charles River	N/A
Mus musculus: Emx1$^{tm1(cre)Krj}$	Jackson Laboratories	RRID:IMSR_JAX:005628
Mus musculus: B6(Cg)-Cux2$^{tm3.1(cre/ERT2)Mull}$/Mmmh	MMRRC	RRID:MMRRC_032779-MU
Mus musculus: Scnn1a-cre3Aibs/J	Jackson Laboratories	RRID:IMSR_JAX:009613
Mus musculus: Tg(Tlx3-cre)PL56Gsat/Mmucd	MMRRC	RRID:MMRRC_041158-UCD
Mus musculus: Ntsr1$^{GN220Gsat/Mmucd}$	MMRRC	RRID:MMRRC_017266-UCD
Mus musculus: Pvalb$^{tm1(cre)Arbr}$	Jackson Laboratories	RRID:IMSR_JAX:008069
Mus musculus: Vip$^{tm1(cre)Zjh}$	Jackson Laboratories	RRID:IMSR_JAX:010908
Mus musculus: Sst$^{tm2.1(cre)Zjh}$	Jackson Laboratories	RRID:IMSR_JAX:018973
Mus musculus: Igs7$^{tm148.1(tetO-GCaMP6f,CAG-tTA2)Hze}$/J	Jackson Laboratories	RRID:IMSR_JAX:030328
Software and algorithms		
MATLAB (2021a)	The MathWorks	RRID:SCR_001622
LabVIEW	National Instruments	RRID:SCR_014325
Python	python.org	RRID:SCR_008394
Panda3D	panda3d.org	N/A

772

773 **Mice.** All animal procedures were approved by and carried out in accordance with guidelines of the
774 Veterinary Department of the Canton Basel-Stadt, Switzerland. The mice used for widefield imaging
775 in this study were kept on a C57BL/6 background and were of the following genotype: 6 C57BL/6
776 (Charles River Laboratories), 4 Emx1-Cre (Gorski et al., 2002), 4 Cux2-CreERT2 (Franco et al., 2012), 7
777 Scnn1a-Cre (Madisen et al., 2010), 22 Tlx3-Cre (Gerfen et al., 2013), 3 Ntsr1-Cre (Gong et al., 2007), 2
778 PV-Cre (Hippenmeyer et al., 2005), 6 VIP-Cre (Taniguchi et al., 2011), and 5 SST-Cre (Taniguchi et al.,
779 2011) mice. Ai148 ((Daigle et al., 2018), Jackson Laboratories, stock #030328) mice were used as
780 breeders to drive GCaMP6f expression in Cre positive neurons. An additional 8 C57BL/6 and 7 Tlx3-
781 Cre mice were used in experiments controlling for hemodynamic responses. To induce expression of
782 Cre in the Cux2-CreERT2 line, mice were provided for at least 1 week with tamoxifen containing food
783 (Envigo, 400 mg tamoxifen per kg of food) as their sole food source. Mice were group housed in a
784 vivarium (light/dark cycle: 12/12 hours). Experimental mice were of either sex.

785 **Surgery and virus injections.** For all surgical procedures, mice were anesthetized using a mixture of
786 fentanyl (0.05 mg/kg; Actavis), midazolam (5.0 mg/kg; Dormicum, Roche), and medetomidine (0.5
787 mg/kg; Domitor, Orion). In a subset of mice (6 C57BL/6, 4 Emx1-Cre, and 4 SST-Cre mice), we
788 injected an AAV vector based on the PHP.eB capsid (Chan et al., 2017) retro-orbitally (6 μl each eye
789 of at least 10^{13} GC/ml) to drive expression of GCaMP under either the EF1α or hSyn1 promoter pan-
790 neuronally, or in a cell type specific manner using a double-floxed inverted open reading frame (DIO)
791 construct. For hemodynamic response control experiments, we used an AAV-PHP.eB-EF1α-eGFP to
792 pan-neuronally express eGFP (**Figures S1A and S1B)** or an AAV-PHP.eB-EF1α-DIO-eGFP to restrict
793 eGFP expression to L5 IT neurons in Tlx3-Cre mice (**Figures S1C and S1D, S5A, S6C-S6E**). To improve
794 optical access to the cortex, we implanted crystal skull cranial windows (Kim et al., 2016). Prior to
795 removing the skull plate overlying dorsal cortex, we recorded the location of bregma relative to
796 other landmarks on the skull. Superglue (Pattex) was used to glue the crystal skull in place in the
797 craniotomy. In a subset of mice, for the comparison of hemodynamic responses (**Figure S1A and**
798 **S1B**), we used a clear skull preparation (Guo et al., 2014). To do this, we attached the crystal skull
799 coverslip directly onto the cleaned skull surface with a three-component polymer (C&B Metabond,
800 Parkell). A custom-machined titanium head bar was attached to the skull using dental cement
801 (Paladur, Heraeus). An epifluorescence overview image was taken to mark reference points on the
802 dorsal cortical surface. Anesthesia was antagonized by an intraperitoneal injection of a mixture of
803 flumazenil (0.5 mg/kg; Anexate, Roche) and atipamezole (2.5 mg/kg; Antisedan, Orion Pharma). For
804 peri- and post-operative analgesia we injected buprenorphine (0.1 mg/kg; Reckitt Benckiser
805 Healthcare (UK) Ltd.) and Metacam (5 mg/kg; Boehringer Ingelheim). Imaging commenced at the

806 earliest 1 week after head bar implantation or 3 weeks after retro-orbital AAV injection. Clozapine
807 (Novartis), aripiprazole (Otsuka Pharmaceutical), haloperidol (Janssen), or amphetamine (Hänseler)
808 was intraperitoneally injected at 0.2 μg/g - 10 μg/g, 0.2 μg/g, 0.1 μg/g or 4 μg/g body weight,
809 respectively.

810 **Virtual reality setup and stimulus design.** For all experiments we used a virtual reality setup as
811 previously described (Leinweber et al., 2014). Mice were head-fixed and free to run on a spherical,
812 air-supported Styrofoam ball. A virtual corridor was projected (using a Samsung SP-F10M projector)
813 onto a toroidal screen positioned in front of the mouse covering a field of view of approximately 240
814 degrees horizontally and 100 degrees vertically. Recordings were blocked into 5-minute sessions.
815 Experiments typically commenced with 4 sessions of a closed loop condition in which the rotation of
816 the spherical treadmill was coupled to the movement in a virtual corridor. To introduce mismatches,
817 we broke the coupling between locomotion and visual flow by briefly halting visual flow for 1 s at
818 random times. Closed loop sessions were followed by 4 sessions of an open loop condition, in which
819 rotation of the spherical treadmill and movement in the virtual corridor were decoupled. The visual
820 stimulus consisted of a replay of the visual flow recorded in the previous closed loop condition.
821 Following this we recorded 2 sessions of what we refer to as a dark condition in which the virtual
822 reality was switched off. Please note, this was not complete darkness, primarily because the
823 shielding of the blue excitation light was not light proof. Finally, we recorded activity in 2 sessions of
824 a grating condition in which we presented drifting grating stimuli (8 directions of 6 s ± 2 s (mean ±
825 SD) duration each with an inter-grating interval of 4.5 s ± 1.5 s (mean ± SD) gray screen, presented in
826 randomized order). These sessions, totaling approximately 1 hour of recording time per day, were
827 acquired for 3 consecutive days. For mice in which we went on to test the effect of drugs on dorsal
828 cortex activity, the first post-drug injection data were acquired +1 h after drug injection (+30 mins in
829 the case of amphetamine because of faster onset kinetics of the drug) and further data were
830 collected at the +24 h and +48 h timepoints. Data in the manuscript are shown as the combined data
831 over either all data collected before drug injection (labelled as naive) or after drug injection (labelled
832 as clozapine, aripiprazole, haloperidol or amphetamine, respectively).

833 **Data acquisition.** All widefield imaging experiments were performed on a custom-built macroscope
834 consisting of commercially available objectives mounted face-to-face (Nikon 85 mm/f1.8 sample
835 side, Nikon 50 mm/f1.4 sensor side). We used a 470 nm LED (Thorlabs) powered by a custom-built
836 LED driver for exciting GCaMP (or eGFP) fluorescence through an excitation filter (SP490, Thorlabs)
837 reflected off a dichroic mirror (LP490, Thorlabs) placed in the parfocal plane of the objectives. Green
838 fluorescence was collected through a 525/50 emission filter on an sCMOS camera (PCO edge 4.2).

839 Apertures on objectives were usually kept maximally open and the current at the LED driver was
840 used to adjust fluorescence intensity to a value that was kept below 25% of the maximum dynamic
841 range of the sensor. In cases where this was not possible (e.g., transfection of eGFP yielded
842 extremely bright fluorescence, often visible with the naked eye), objective apertures were gradually
843 reduced to avoid overexposure of the sensor. LED illumination was adjusted with a collimator
844 (Thorlabs SM2F32-A) to achieve homogenous illumination across the surface of the cranial window.
845 The resulting Gaussian profile of the illumination cone was further trimmed with black tape on the
846 sample side objective to avoid light shining directly into the mouse's eye. An Arduino board (Arduino
847 Mega 2560) was used to control LED onsets synced to the frame trigger signal of the camera. The
848 duty cycle of the 470 nm LED was 90%. Raw images were acquired at full speed (100 Hz; except for
849 eGFP controls, which were acquired at 50 Hz effective frame rate) and full dynamic range (16 bit) of
850 the sensor. The raw images were cropped on-sensor and the resulting data was streamed to disk
851 with custom written software in LabVIEW (National Instruments), resulting in an effective pixel size
852 of 60 μm^2 at a standardized imaging resolution of 1108 pixels x 1220 pixels (1.35 MP).

853 Two-photon calcium imaging was performed using a custom-built microscope based on a Thorlabs B-
854 scope (Leinweber et al., 2014). Illumination source was a tunable femtosecond laser (Coherent
855 Chameleon) tuned to 930 nm. Emission light was band-pass filtered using a 525/50 filter for GCaMP
856 and detected using a GaAsP photomultiplier (H7422, Hamamatsu). Photomultiplier signals were
857 amplified (DHPCA-100, Femto), digitized (NI5772, National Instruments) at 800 MHz, and band-pass
858 filtered around 80 MHz using a digital Fourier-transform filter implemented in custom-written
859 software on an FPGA (NI5772, National Instruments). The scanning system of the microscope was
860 based on a 12 kHz resonant scanner (Cambridge Technology). Images were acquired at a resolution
861 of 750 pixels x 400 pixels at a 60 Hz frame rate and a piezo-electric linear actuator (P-726, Physik
862 Instrumente) was used to move the objective (Nikon 16x, 0.8 NA) in steps of 15 µm between frames
863 to acquire images at 4 different depths. This resulted in an effective frame rate of 15 Hz. The field of
864 view was 350 µm x 350 µm.

865 **Data processing.** Off-line data processing and data analysis (section below) were done with custom-
866 written MATLAB (2021a) scripts. For widefield macroscope imaging, raw movie data was manually
867 registered across days by aligning subsequent mean projections of the data to the first recorded
868 image sequence. We placed regions of interest (ROIs) relative to readily identifiable anatomical
869 landmarks that had been previously noted during cranial window surgery (see above). This resulted
870 in the selection of six 20 pixels x 20 pixels ROIs per hemisphere. Of those ROIs, we calculated the
871 activity as the $\Delta F/F_0$, wherein F_0 was the median fluorescence of the recording (approximately

872 30 000 frames in a 5 min recording). $\Delta F/F_0$ was corrected for slow fluorescence drift caused by
873 thermal brightening of the LED using 8th percentile filtering with a 62.5 s moving window similar to
874 what was described previously for two-photon imaging (Daniel A. Dombeck et al., 2007).

875 Raw two-photon imaging data were full-frame registered to correct for brain motion. Neurons were
876 manually selected based on mean and maximum fluorescence images. Raw fluorescence traces were
877 corrected for slow drift in fluorescence using an 8th percentile filtering with a 15 s window (Daniel A
878 Dombeck et al., 2007). ΔF/F traces were calculated as mean fluorescence in a selected region of
879 every imaging frame and subsequently subtracted and normalized by the median fluorescence.

880 **Data analysis.** Locomotion and visual flow onsets were determined based on threshold crossing of
881 locomotion or visual flow speed. To select only well isolated onsets, we used a speed threshold of 30
882 cm/s and excluded all onsets with locomotion or visual flow in the 3 s window preceding the onset.
883 To increase the number of locomotion onsets that passed the speed threshold criterion for the eGFP
884 imaging data (**Figures S1, S5A**), we excluded only those onsets if there was locomotion in the 1 s
885 window preceding onset.

886 All stimulus response curves (**Figures 1F-1L, 3B and 3C, 3E and 3F, 4, 8, S1-S4, S5A and S5B, S5E and**
887 **S5F**) were baseline subtracted. The baseline subtraction window for unpredictable stimuli
888 (mismatches and grating onsets) was -200 ms to 0 ms before stimulus onset. For closed loop and
889 open loop locomotion onsets, and open loop visual flow onsets, to accommodate calcium indicator
890 offset dynamics and potential anticipatory activity, we placed the baseline subtraction windows for
891 these onsets at -2900 ms to -2700 ms for GCaMP imaging, or -900 ms to -700 ms for eGFP imaging.
892 Varying this window within the bounds of offset dynamics of the indicator and anticipatory activity
893 onset did not change the conclusions drawn in this manuscript. Analyses in which image sequences
894 were aligned to event onsets (**Figures 1C-1D and 3**) used the same parameters as above.

895 On rare occasions, we observed seizure-like activity after antipsychotic drug injection. These events
896 resulted in atypically high levels of correlation, and to avoid them from influencing our conclusions
897 we excluded these data from further analysis. We excluded sessions if they contained an event in
898 which average activity of all 12 ROIs remained elevated above 30% ΔF/F for more than 10 s. This
899 criterion led to the exclusion of 0.26% of data (10 out of 3801 of 5 min recording sessions).

900 To quantify the similarity of closed loop and open loop locomotion onset responses shown in **Figure**
901 **1L** we calculated the correlation coefficient between the averaged responses (onsets and mice, 1 s
902 moving average) in a window -5 s to +3 s, for each ROI.

903 To calculate the maps that show the timing of activation of individual dorsal cortex regions (**Figures**
904 **3B and 3C, 3E and 3F**), we first aligned the craniotomies of all mice within one genotype to the first
905 mouse's average grating response map and then calculated an average dorsal cortex response time
906 course. For each pixel of this image sequence, we then determined the time at which the pixel's
907 value crossed a threshold of the maximum value in the entire time course, divided by 6 standard
908 deviations of the pixel's baseline value (-200 ms to 0 ms before event onset, as stated above). The
909 resulting maps were denoised using a Gaussian filter and we removed all pixel clusters that
910 contained fewer than 500 connected pixels. For illustration purposes, these maps were overlaid over
911 an example crystal skull craniotomy to produce the panels shown in **Figure 3**.

912 For the correlation analyses shown in **Figures 5-7, S6-S8**, we first calculated the correlation
913 coefficient of neuronal activity (or fluorescence change, in the case of Tlx3-Cre mice that had been
914 retro-orbitally injected with an AAV-PHP.eB-Ef1α-DIO-eGFP to express eGFP in L5 IT neurons) for all
915 possible pairs of the 12 regions of interest. We then determined the distance between each pair of
916 ROIs and normalized this value by the distance between bregma and lambda obtained from the
917 images during initial surgery for each mouse (**Figure S6A**). We plotted the correlation against the
918 distance for each pair of regions of interest and binned the data in a 40 x 40 grid and smoothed the
919 resulting image with a gaussian filter (**Figure S6B**), to obtain the heatmaps shown in **Figures 6A and**
920 **6B, 6D and 6E, 7A and 7B, 7D and 7E, 7G and 7H, S6B-S6D, S7A and S7B, S8C and S8D**. Contour lines
921 in the heatmaps were then drawn to 50% of the maximum value in the plot. The boxplot
922 quantifications (**Figures 6C, 6F, 7C, 7F, 7I, S6E, S7C, S8E**) were calculated as the change in correlation
923 coefficient of activity after and before treatment for all pairs of regions of interest, normalized to the
924 value before treatment and split into short- and long-range using a threshold of 0.9 of the bregma-
925 lambda distance for each mouse. For pairwise neuronal correlations that had been recorded with
926 two-photon imaging (**Figure S7D**), we calculated the correlation coefficient separately for all pairs of
927 neurons within each field of view. We noticed extreme synchrony of activity of L5 IT soma recorded
928 in 1 field of view with two-photon imaging after clozapine injection and show, both distributions for
929 all data, as well as the distribution when this 1 field of view is excluded.

930 For **Figure S2,** onset aligned data were first averaged for each mouse and then summed in the given
931 combinations. The SEM was calculated over mice.

932 To obtain the differences in the correlation between activity and locomotion after and before
933 clozapine injection (**Figure S5D**), we first averaged all correlation coefficients in the individual
934 sessions of a condition (closed loop, open loop, or dark) to generate one correlation coefficient per

935 mouse and ROI, for each condition. We then calculated and plotted the difference between these
936 correlation values after and before clozapine injection.

937 ACKNOWLEDGEMENTS

938 We thank Tingjia Lu for production of the AAV vectors, Rebecca Jordan for performing the clear skull
939 implants used in the hemodynamic response measurements, and members of the Keller lab for
940 discussion and support. This project has received funding from the Swiss National Science
941 Foundation, the Novartis Research Foundation, and the European Research Council (ERC) under the
942 European Union's Horizon 2020 research and innovation programme (grant agreement No 865617).

943 AUTHOR CONTRIBUTIONS

944 MH performed the experiments and analyzed the data. All authors wrote the manuscript.

945 CONFLICT OF INTEREST

946 Part of the results presented herein have been included in patent application EP22153051.1.

REFERENCES

Allen, W.E., Kauvar, I.V., Chen, M.Z., Richman, E.B., Yang, S.J., Chan, K., Gradinaru, V., Deverman, B.E., Luo, L., Deisseroth, K., 2017. Global Representations of Goal-Directed Behavior in Distinct Cell Types of Mouse Neocortex. Neuron 94, 891-907.e6. https://doi.org/10.1016/j.neuron.2017.04.017

Anderson, C.T., Sheets, P.L., Kiritani, T., Shepherd, G.M.G., 2010. Sublayer-specific microcircuits of corticospinal and corticostriatal neurons in motor cortex. Nat Neurosci 13, 739–744. https://doi.org/10.1038/nn.2538

Aravanis, A.M., Wang, L.-P., Zhang, F., Meltzer, L.A., Mogri, M.Z., Schneider, M.B., Deisseroth, K., 2007. An optical neural interface: in vivo control of rodent motor cortex with integrated fiberoptic and optogenetic technology. J Neural Eng 4, S143-156. https://doi.org/10.1088/1741-2560/4/3/S02

Attinger, A., Wang, B., Keller, G.B., 2017. Visuomotor Coupling Shapes the Functional Development of Mouse Visual Cortex. Cell 169, 1291-1302.e14. https://doi.org/10.1016/j.cell.2017.05.023

Audette, N.J., Zhou, W., Schneider, D.M., 2021. Temporally precise movement-based predictions in the mouse auditory cortex. https://doi.org/10.1101/2021.12.13.472457

Ayaz, A., Stäuble, A., Hamada, M., Wulf, M.A., Saleem, A.B., Helmchen, F., 2019. Layer-specific integration of locomotion and sensory information in mouse barrel cortex. Nature Communications 10, 1–14. https://doi.org/10.1038/s41467-019-10564-8

Bastos, A.M., Usrey, W.M., Adams, R.A., Mangun, G.R., Fries, P., Friston, K.J., 2012. Canonical microcircuits for predictive coding. Neuron 76, 695–711. https://doi.org/10.1016/j.neuron.2012.10.038

Catafau, A.M., Parellada, E., Lomeña, F.J., Bernardo, M., Pavía, J., Ros, D., Setoain, J., Gonzalez-Monclús, E., 1994. Prefrontal and temporal blood flow in schizophrenia: resting and activation technetium-99m-HMPAO SPECT patterns in young neuroleptic-naive patients with acute disease. J Nucl Med 35, 935–941.

Chan, K.Y., Jang, M.J., Yoo, B.B., Greenbaum, A., Ravi, N., Wu, W.-L., Sánchez-Guardado, L., Lois, C., Mazmanian, S.K., Deverman, B.E., Gradinaru, V., 2017. Engineered AAVs for efficient noninvasive gene delivery to the central and peripheral nervous systems. Nat Neurosci 20, 1172–1179. https://doi.org/10.1038/nn.4593

Chen, X., Sun, Y.-C., Zhan, H., Kebschull, J.M., Fischer, S., Matho, K., Huang, Z.J., Gillis, J., Zador, A.M., 2019. High-Throughput Mapping of Long-Range Neuronal Projection Using In Situ Sequencing. Cell 179, 772-786.e19. https://doi.org/10.1016/j.cell.2019.09.023

Constantinople, C.M., Bruno, R.M., 2013. Deep cortical layers are activated directly by thalamus. Science (New York, N.Y.) 340, 1591–1594. https://doi.org/10.1126/science.1236425

Daigle, T.L., Madisen, L., Hage, T.A., Valley, M.T., Knoblich, U., Larsen, R.S., Takeno, M.M., Huang, L., Gu, H., Larsen, R., Mills, M., Bosma-Moody, A., Siverts, L.A., Walker, M., Graybuck, L.T., Yao, Z., Fong, O., Nguyen, T.N., Garren, E., Lenz, G.H., Chavarha, M., Pendergraft, J., Harrington, J., Hirokawa, K.E., Harris, J.A., Nicovich, P.R., McGraw, M.J., Ollerenshaw, D.R., Smith, K.A., Baker, C.A., Ting, J.T., Sunkin, S.M., Lecoq, J., Lin, M.Z., Boyden, E.S., Murphy, G.J., da Costa, N.M., Waters, J., Li, L., Tasic, B., Zeng, H., 2018. A Suite of Transgenic Driver and Reporter Mouse Lines with Enhanced Brain-Cell-Type Targeting and Functionality. Cell 174, 465-480.e22. https://doi.org/10.1016/j.cell.2018.06.035

Dierks, T., Linden, D.E., Jandl, M., Formisano, E., Goebel, R., Lanfermann, H., Singer, W., 1999. Activation of Heschl's gyrus during auditory hallucinations. Neuron 22, 615–621. https://doi.org/10.1016/s0896-6273(00)80715-1

Dombeck, Daniel A., Khabbaz, A.N., Collman, F., Adelman, T.L., Tank, D.W., 2007. Imaging large-scale neural activity with cellular resolution in awake, mobile mice. Neuron 56, 43–57. https://doi.org/10.1016/j.neuron.2007.08.003

Dombeck, Daniel A, Khabbaz, A.N., Collman, F., Adelman, T.L., Tank, D.W., 2007. Imaging large-scale neural activity with cellular resolution in awake, mobile mice. Neuron 56, 43–57. https://doi.org/10.1016/j.neuron.2007.08.003

Douglas, R.J., Martin, K.A., 1991. A functional microcircuit for cat visual cortex. The Journal of Physiology 440, 735–769. https://doi.org/10.1113/jphysiol.1991.sp018733

Eliades, S.J., Wang, X., 2008. Neural substrates of vocalization feedback monitoring in primate auditory cortex. Nature 453, 1102–6. https://doi.org/10.1038/nature06910

Fletcher, P.C., Frith, C.D., 2009. Perceiving is believing: a Bayesian approach to explaining the positive symptoms of schizophrenia. Nature reviews. Neuroscience 10, 48–58. https://doi.org/10.1038/nrn2536

Franco, S.J., Gil-Sanz, C., Martinez-Garay, I., Espinosa, A., Harkins-Perry, S.R., Ramos, C., Müller, U., 2012. Fate-Restricted Neural Progenitors in the Mammalian Cerebral Cortex. Science. https://doi.org/10.1126/science.1223616

Frith, C., 2005. The neural basis of hallucinations and delusions. Comptes rendus biologies 328, 169–75.

Garner, A.R., Keller, G.B., 2022. A cortical circuit for audio-visual predictions. Nat Neurosci 25, 98–105. https://doi.org/10.1038/s41593-021-00974-7

Gerfen, C.R., Paletzki, R., Heintz, N., 2013. GENSAT BAC Cre-Recombinase Driver Lines to Study the Functional Organization of Cerebral Cortical and Basal Ganglia Circuits. Neuron 80, 1368–1383. https://doi.org/10.1016/j.neuron.2013.10.016

Gong, S., Doughty, M., Harbaugh, C.R., Cummins, A., Hatten, M.E., Heintz, N., Gerfen, C.R., 2007. Targeting Cre Recombinase to Specific Neuron Populations with Bacterial Artificial Chromosome Constructs. J. Neurosci. 27, 9817–9823.

Gorski, J.A., Talley, T., Qiu, M., Puelles, L., Rubenstein, J.L.R., Jones, K.R., 2002. Cortical excitatory neurons and glia, but not GABAergic neurons, are produced in the Emx1-expressing lineage. J Neurosci 22, 6309–6314. https://doi.org/20026564

Guo, Z.V., Li, N., Huber, D., Ophir, E., Gutnisky, D., Ting, J.T., Feng, G., Svoboda, K., 2014. Flow of cortical activity underlying a tactile decision in mice. Neuron 81, 179–194. https://doi.org/10.1016/j.neuron.2013.10.020

Haarsma, J., Kok, P., Browning, M., 2020. The promise of layer-specific neuroimaging for testing predictive coding theories of psychosis. Schizophrenia Research. https://doi.org/10.1016/j.schres.2020.10.009

Harris, J.A., Mihalas, S., Hirokawa, K.E., Whitesell, J.D., Choi, H., Bernard, A., Bohn, P., Caldejon, S., Casal, L., Cho, A., Feiner, A., Feng, D., Gaudreault, N., Gerfen, C.R., Graddis, N., Groblewski, P.A., Henry, A.M., Ho, A., Howard, R., Knox, J.E., Kuan, L., Kuang, X., Lecoq, J., Lesnar, P., Li, Y., Luviano, J., McConoughey, S., Mortrud, M.T., Naeemi, M., Ng, L., Oh, S.W., Ouellette, B., Shen, E., Sorensen, S.A., Wakeman, W., Wang, Q., Wang, Y., Williford, A., Phillips, J.W., Jones, A.R., Koch, C., Zeng, H., 2019. Hierarchical organization of cortical and thalamic connectivity. Nature 575, 195–202. https://doi.org/10.1038/s41586-019-1716-z

Harrison, P.J., Weinberger, D.R., 2005. Schizophrenia genes, gene expression, and neuropathology: on the matter of their convergence. Mol Psychiatry 10, 40–68. https://doi.org/10.1038/sj.mp.4001558

Heindorf, M., Arber, S., Keller, G.B., 2018. Mouse Motor Cortex Coordinates the Behavioral Response to Unpredicted Sensory Feedback. Neuron 99, 1040-1054.e5. https://doi.org/10.1016/j.neuron.2018.07.046

Hippenmeyer, S., Vrieseling, E., Sigrist, M., Portmann, T., Laengle, C., Ladle, D.R., Arber, S., 2005. A Developmental Switch in the Response of DRG Neurons to ETS Transcription Factor Signaling. PLOS Biology 3, e159. https://doi.org/10.1371/journal.pbio.0030159

Javitt, D.C., 2009. Sensory Processing in Schizophrenia: Neither Simple nor Intact. Schizophr Bull 35, 1059–1064. https://doi.org/10.1093/schbul/sbp110

Jiang, L.P., Rao, R.P.N., 2021. Predictive Coding Theories of Cortical Function. arXiv:2112.10048 [q-bio].

Jordan, M.I., Rumelhart, D.E., 1992. Forward Models: Supervised Learning with a Distal Teacher. Cognitive Science 16, 307–354. https://doi.org/10.1207/s15516709cog1603_1

Jordan, R., Keller, G.B., 2020. Opposing Influence of Top-down and Bottom-up Input on Excitatory Layer 2/3 Neurons in Mouse Primary Visual Cortex. Neuron 108, 1194-1206.e5. https://doi.org/10.1016/j.neuron.2020.09.024

Keller, G.B., Bonhoeffer, T., Hübener, M., 2012. Sensorimotor mismatch signals in primary visual cortex of the behaving mouse. Neuron 74, 809–15. https://doi.org/10.1016/j.neuron.2012.03.040

Keller, G.B., Hahnloser, R.H.R., 2009. Neural processing of auditory feedback during vocal practice in a songbird. Nature 457, 187–90. https://doi.org/10.1038/nature07467

Keller, G.B., Mrsic-Flogel, T.D., 2018. Predictive Processing: A Canonical Cortical Computation. Neuron 100, 424–435. https://doi.org/10.1016/j.neuron.2018.10.003

Kim, T.H., Zhang, Y., Lecoq, J., Jung, J.C., Li, J., Zeng, H., Niell, C.M., Schnitzer, M.J., 2016. Long-Term Optical Access to an Estimated One Million Neurons in the Live Mouse Cortex. Cell Rep 17, 3385–3394. https://doi.org/10.1016/j.celrep.2016.12.004

Kiritani, T., Wickersham, I.R., Seung, H.S., Shepherd, G.M.G., 2012. Hierarchical connectivity and connection-specific dynamics in the corticospinal-corticostriatal microcircuit in mouse motor cortex. J Neurosci 32, 4992–5001. https://doi.org/10.1523/JNEUROSCI.4759-11.2012

Le Bihan, D., Turner, R., Zeffiro, T.A., Cuénod, C.A., Jezzard, P., Bonnerot, V., 1993. Activation of human primary visual cortex during visual recall: a magnetic resonance imaging study. Proceedings of the National Academy of Sciences of the United States of America 90, 11802–5.

Leinweber, M., Ward, D.R., Sobczak, J.M., Attinger, A., Keller, G.B., 2017. A Sensorimotor Circuit in Mouse Cortex for Visual Flow Predictions. Neuron 95, 1420-1432.e5. https://doi.org/10.1016/j.neuron.2017.08.036

Leinweber, M., Zmarz, P., Buchmann, P., Argast, P., Hübener, M., Bonhoeffer, T., Keller, G.B., 2014. Two-photon calcium imaging in mice navigating a virtual reality environment. Journal of visualized experiments : JoVE e50885.

Li, S., Hu, N., Zhang, W., Tao, B., Dai, J., Gong, Y., Tan, Y., Cai, D., Lui, S., 2019. Dysconnectivity of Multiple Brain Networks in Schizophrenia: A Meta-Analysis of Resting-State Functional Connectivity. Front. Psychiatry 0. https://doi.org/10.3389/fpsyt.2019.00482

Li, T., Wang, Q., Zhang, J., Rolls, E.T., Yang, W., Palaniyappan, L., Zhang, L., Cheng, W., Yao, Y., Liu, Zhaowen, Gong, X., Luo, Q., Tang, Y., Crow, T.J., Broome, M.R., Xu, K., Li, C., Wang, J., Liu, Zhening, Lu, G., Wang, F., Feng, J., 2017. Brain-Wide Analysis of Functional Connectivity in First-Episode and Chronic Stages of Schizophrenia. Schizophr Bull 43, 436–448. https://doi.org/10.1093/schbul/sbw099

Ma, Y., Shaik, M.A., Kim, S.H., Kozberg, M.G., Thibodeaux, D.N., Zhao, H.T., Yu, H., Hillman, E.M.C., 2016. Wide-field optical mapping of neural activity and brain haemodynamics: considerations and novel approaches. Philosophical Transactions of the Royal Society B: Biological Sciences 371, 20150360. https://doi.org/10.1098/rstb.2015.0360

Madisen, L., Zwingman, T.A., Sunkin, S.M., Oh, S.W., Zariwala, H.A., Gu, H., Ng, L.L., Palmiter, R.D., Hawrylycz, M.J., Jones, A.R., Lein, E.S., Zeng, H., 2010. A robust and high-throughput Cre reporting and characterization system for the whole mouse brain. Nature Neuroscience 13, 133–140. https://doi.org/10.1038/nn.2467

Maia, T.V., Frank, M.J., 2017. An Integrative Perspective on the Role of Dopamine in Schizophrenia. Biol Psychiatry 81, 52–66. https://doi.org/10.1016/j.biopsych.2016.05.021

1094 Moghaddam, B., Javitt, D., 2012. From Revolution to Evolution: The Glutamate Hypothesis of
1095 Schizophrenia and its Implication for Treatment. Neuropsychopharmacol 37, 4–15.
1096 https://doi.org/10.1038/npp.2011.181
1097 Morita, K., Im, S., Kawaguchi, Y., 2019. Differential Striatal Axonal Arborizations of the
1098 Intratelencephalic and Pyramidal-Tract Neurons: Analysis of the Data in the MouseLight
1099 Database. Frontiers in Neural Circuits 13.
1100 Musall, S., Kaufman, M.T., Juavinett, A.L., Gluf, S., Churchland, A.K., 2019. Single-trial neural
1101 dynamics are dominated by richly varied movements. Nat Neurosci 22, 1677–1686.
1102 https://doi.org/10.1038/s41593-019-0502-4
1103 Northoff, G., Duncan, N.W., 2016. How do abnormalities in the brain's spontaneous activity translate
1104 into symptoms in schizophrenia? From an overview of resting state activity findings to a
1105 proposed spatiotemporal psychopathology. Prog Neurobiol 145–146, 26–45.
1106 https://doi.org/10.1016/j.pneurobio.2016.08.003
1107 Oberlaender, M., Ramirez, A., Bruno, R.M., 2012. Sensory Experience Restructures Thalamocortical
1108 Axons during Adulthood. Neuron 74, 648–655.
1109 https://doi.org/10.1016/j.neuron.2012.03.022
1110 Pakan, J.M., Lowe, S.C., Dylda, E., Keemink, S.W., Currie, S.P., Coutts, C.A., Rochefort, N.L., 2016.
1111 Behavioral-state modulation of inhibition is context-dependent and cell type specific in
1112 mouse visual cortex. eLife 5. https://doi.org/10.7554/eLife.14985
1113 Parellada, M., Gomez-Vallejo, S., Burdeus, M., Arango, C., 2017. Developmental Differences Between
1114 Schizophrenia and Bipolar Disorder. Schizophr Bull 43, 1176–1189.
1115 https://doi.org/10.1093/schbul/sbx126
1116 Rao, R.P.N., Ballard, D.H., 1999. Predictive coding in the visual cortex: a functional interpretation of
1117 some extra-classical receptive-field effects. Nature Neuroscience 2, 79–87.
1118 https://doi.org/10.1038/4580
1119 Saleem, A.B., Ayaz, A., Jeffery, K.J., Harris, K.D., Carandini, M., 2013. Integration of visual motion and
1120 locomotion in mouse visual cortex. Nature neuroscience 16, 1864–9.
1121 https://doi.org/10.1038/nn.3567
1122 Schmack, K., Bosc, M., Ott, T., Sturgill, J.F., Kepecs, A., 2021. Striatal dopamine mediates
1123 hallucination-like perception in mice. Science 372, eabf4740.
1124 https://doi.org/10.1126/science.abf4740
1125 Schneider, D.M., Sundararajan, J., Mooney, R., 2018. A cortical filter that learns to suppress the
1126 acoustic consequences of movement. Nature 561, 391–395.
1127 https://doi.org/10.1038/s41586-018-0520-5
1128 Shergill, S.S., Brammer, M.J., Williams, S.C., Murray, R.M., McGuire, P.K., 2000. Mapping auditory
1129 hallucinations in schizophrenia using functional magnetic resonance imaging. Arch Gen
1130 Psychiatry 57, 1033–1038. https://doi.org/10.1001/archpsyc.57.11.1033
1131 Singh, T., Neale, B.M., Daly, M.J., Consortium, on behalf of the S.E.M.-A. (SCHEMA), 2020. Exome
1132 sequencing identifies rare coding variants in 10 genes which confer substantial risk for
1133 schizophrenia. https://doi.org/10.1101/2020.09.18.20192815
1134 Stanley, J., Miall, R.C., 2007. Functional activation in parieto-premotor and visual areas dependent
1135 on congruency between hand movement and visual stimuli during motor-visual priming.
1136 NeuroImage 34, 290–9. https://doi.org/10.1016/j.neuroimage.2006.08.043
1137 Stringer, C., Pachitariu, M., Steinmetz, N., Reddy, C.B., Carandini, M., Harris, K.D., 2019. Spontaneous
1138 behaviors drive multidimensional, brainwide activity. Science 364, 255.
1139 https://doi.org/10.1126/science.aav7893
1140 Suzuki, M., Larkum, M.E., 2020. General Anesthesia Decouples Cortical Pyramidal Neurons. Cell 180,
1141 666-676.e13. https://doi.org/10.1016/j.cell.2020.01.024
1142 Taniguchi, H., He, M., Wu, P., Kim, S., Paik, R., Sugino, K., Kvitsani, D., Fu, Y., Lu, J., Lin, Y., Miyoshi, G.,
1143 Shima, Y., Fishell, G., Nelson, S.B., Huang, Z.J., 2011. A Resource of Cre Driver Lines for

Genetic Targeting of GABAergic Neurons in Cerebral Cortex. Neuron 71, 995–1013. https://doi.org/10.1016/j.neuron.2011.07.026

Valley, M.T., Moore, M.G., Zhuang, J., Mesa, N., Castelli, D., Sullivan, D., Reimers, M., Waters, J., 2020. Separation of hemodynamic signals from GCaMP fluorescence measured with wide-field imaging. J Neurophysiol 123, 356–366. https://doi.org/10.1152/jn.00304.2019

Wekselblatt, J.B., Flister, E.D., Piscopo, D.M., Niell, C.M., 2016. Large-scale imaging of cortical dynamics during sensory perception and behavior. Journal of Neurophysiology 115, 2852–2866. https://doi.org/10.1152/jn.01056.2015

Widmer, F.C., Keller, G.B., 2021. Developmental plasticity in visual cortex is necessary for normal visuomotor integration and visuomotor skill learning. bioRxiv 2021.06.20.449148. https://doi.org/10.1101/2021.06.20.449148

Xu, X., Olivas, N.D., Ikrar, T., Peng, T., Holmes, T.C., Nie, Q., Shi, Y., 2016. Primary visual cortex shows laminar-specific and balanced circuit organization of excitatory and inhibitory synaptic connectivity. The Journal of Physiology 594, 1891–1910. https://doi.org/10.1113/JP271891

Yamawaki, N., Shepherd, G.M.G., 2015. Synaptic circuit organization of motor corticothalamic neurons. J Neurosci 35, 2293–2307. https://doi.org/10.1523/JNEUROSCI.4023-14.2015

Yoon, J.H., Rokem, A.S., Silver, M.A., Minzenberg, M.J., Ursu, S., Ragland, J.D., Carter, C.S., 2009. Diminished orientation-specific surround suppression of visual processing in schizophrenia. Schizophr Bull 35, 1078–1084. https://doi.org/10.1093/schbul/sbp064

Zmarz, P., Keller, G.B., 2016. Mismatch Receptive Fields in Mouse Visual Cortex. Neuron 92, 766–772. https://doi.org/10.1016/j.neuron.2016.09.057